JGR Earth Surface

RESEARCH ARTICLE
10.1029/2022JF006673

Radar Characterization of Ice Crystal Orientation Fabric and Anisotropic Viscosity Within an Antarctic Ice Stream

T. M. Jordan[1,2,3], C. Martín[4], A. M. Brisbourne[4], D. M. Schroeder[3,5], and A. M. Smith[4]

[1]Plymouth Marine Laboratory, Plymouth, UK, [2]School of Geographical Sciences, University of Bristol, Bristol, UK, [3]Department of Geophysics, Stanford University, Stanford, CA, USA, [4]British Antarctic Survey, Cambridge, UK, [5]Department of Electrical Engineering, Stanford University, Stanford, CA, USA

Key Points:

- Pronounced spatial variability of ice crystal orientation fabric is inferred from radar sounding in the near surface of Rutford Ice Stream
- In the shallowest ice, the fabric is generally aligned with surface compression whereas in deeper ice this is not always the case
- The fabric results in lateral and depth variations of anisotropic ice viscosity within the flow unit including sharp depth transitions

Supporting Information:

Supporting Information may be found in the online version of this article.

Correspondence to:

T. M. Jordan and C. Martín,
tjor@pml.ac.uk;
cama@bas.ac.uk

Citation:

Jordan, T. M., Martín, C., Brisbourne, A. M., Schroeder, D. M., & Smith, A. M. (2022). Radar characterization of ice crystal orientation fabric and anisotropic viscosity within an Antarctic ice stream. *Journal of Geophysical Research: Earth Surface*, *127*, e2022JF006673. https://doi.org/10.1029/2022JF006673

Received 15 MAR 2022
Accepted 1 JUN 2022

Abstract We use polarimetric radar sounding to investigate ice crystal orientation fabric and its impact on ice viscosity within the near surface of Rutford Ice Stream, West Antarctica. The technique retrieves lateral and depth variations in the horizontal components of ice fabric but no direct information on the vertical fabric component. In the shallowest ice (depths 40–100 m), the fabric is consistent with flow-induced development and correlates with the surface compression direction. Notably, toward the ice-stream margin, the horizontal compression angle and azimuthal fabric orientation tend toward 45° relative to ice flow which is consistent with the early stages of flow-induced fabric under simple shear. The fabric orientation in deeper ice (depths 100–300 m) is, in places, significantly misaligned with shallower ice and the surface compression direction due to sharp depth transitions in orientation. We then use a rheological model to bound effective anisotropic viscosities (directional hardness) of ice that are consistent with the radar measurements. Toward the shear margin, we show that the shallow-ice fabric does not appreciably soften the ice to lateral shear although this may happen in deeper ice. In the center of the ice stream, we show that lateral and depth variations in the fabric alignment relative to ice flow result in corresponding changes in uniaxial ice viscosities relative to ice flow. Our results indicate that spatial variability in the fabric translates to variability in viscosity that widely used isotropic ice-flow models are unable to consider.

Plain Language Summary The viscosity of glacier ice is dependent on the direction in which ice crystals are pointing relative to an applied load. This ice crystal orientation fabric also contains information about past ice flow. Compared with the interior of ice sheets, the relationships between fabric, viscosity, and ice flow are relatively unexplored in the ice streams and outlet glaciers which drain the Antarctic Ice Sheet. We use a ground-based geophysical method to investigate how ice fabric varies spatially within Rutford Ice Stream (West Antarctica) and then calculate the relative viscosity of ice for deformation in different directions. Our results reveal rapidly varying fabric properties within the flow unit. In the shallowest ice, the fabric is consistent with what would be expected from the surface deformation, whereas in deeper ice, this is not always true. We then show that spatial variation in ice fabric translates to lateral and depth variations in directional ice viscosity. This poses challenges for using ice-flow models to derive glacier bed conditions as they do not generally account for directional viscosity.

1. Introduction

The flow of glacier ice is controlled by its rheology, which determines how ice deforms under an applied stress. A range of rheological factors influence the effective viscosity of ice, including temperature, microstructural properties, such as ice crystal orientation fabric and grain size, damage to the ice, and the character of the underlying stress regime (Cuffey & Paterson, 2010). The ice crystal orientation fabric, from herein referred to as "fabric," describes the orientation distribution of ice crystals in relation to their crystallographic axes (c-axes). The ice fabric is the primary control on anisotropic viscosity (i.e., when the viscosity of ice is softer or harder for different stress components). In addition to influencing present-day deformation, the ice fabric encodes strain history due to the rotation of the c-axes toward the compressive strain axis (direction of least extension) (Azuma & Higashi, 1985; R. B. Alley, 1988; Wang et al., 2002).

To model the influence of fabric on ice flow, a range of anisotropic flow laws for polycrystalline ice have been developed. These flow laws include a tensorial relationship for bulk ice viscosity (or its inverse, fluidity) derived from the fabric state (Azuma & Goto-Azuma, 1996; Budd et al., 2013; Faria et al., 2014; Gagliardini et al., 2009;

Gillet-Chaulet et al., 2005; Godert, 2003), scalar enhancement derived from the fabric state (Staroszczyk & Morland, 2000), and empirical parameterization based on the stress field (Budd et al., 2013; Graham et al., 2018). In both tensorial and scalar formulations, anisotropic flow laws demonstrate that the fabric can have a pronounced effect on large-scale ice-sheet flow (Graham et al., 2018; Ma et al., 2010). However, primarily due to the scarcity of measurements, it is often unclear how ice fabric and its spatial variability impact on ice flow and stability across the ice sheets.

The effects of ice fabric and anisotropic viscosity on ice-sheet flow are best characterized at slow-flowing divides and domes where there are often direct fabric measurements available from ice cores (e.g., Kluskiewicz et al., 2017; Montagnat et al., 2014). At ice domes, deformation is dominated by vertical compression, which induces a fabric where the c-axes cluster in the vertical direction, which is often referred to as a vertical pole or single maximum fabric. A vertical pole fabric results in anisotropic ice being softer to horizontal shearing (vertical gradients in horizontal velocity), and harder to vertical compression, than isotropic ice (Azuma & Goto-Azuma, 1996; Thorsteinsson et al., 1997), the latter property impacting on the age-depth relationship (Martin et al., 2009; Pettit et al., 2007). As horizontal shearing dominates the deformation of grounded ice, pole-like fabrics are predicted to result in significant enhancement of ice flow across an ice sheet (Ma et al., 2010). At ice divides, where there is horizontal extension present, vertical girdle fabrics (*c*-axes orientated in a plane perpendicular to the extension direction) develop at moderate ice depths (Kluskiewicz et al., 2017; Montagnat et al., 2014; Wang et al., 2002). Vertical girdle fabrics are predicted to harden ice to extension relative to isotropic ice (Ma et al., 2010).

In fast-flowing ice streams, there are fewer direct measurements of ice fabric available, and geophysical techniques, including passive seismics (Smith et al., 2017), active seismics (Picotti et al., 2015), radar sounding (Jordan, Schroeder, et al., 2020), provide an alternative means to measure fabrics. Taken together, ice stream fabric measurements demonstrate distinct variability with fabrics that approximate single-pole, multiple-pole, girdle, and random states all present in different geophysical surveys (Horgan et al., 2011; Jackson & Kamb, 1997; Jordan, Schroeder, et al., 2020; Picotti et al., 2015; Smith et al., 2017). We typically expect lateral shear (horizontal gradients in horizontal velocity) to dominate the near-surface deformation at ice stream margins with along-flow extension becoming important in the center of the ice stream. However, this picture is an oversimplification and ice streams also exhibit "ice-flow complexity" with alternating bands of flow convergence and divergence (Ng, 2015) and along-flow compression (Minchew et al., 2016) often present. In correspondence with variable deformation behavior, anisotropic viscosity is also anticipated to vary within ice streams. For example, Minchew et al. (2018) inferred that the ice fabric has a softening effect on lateral shear within the margins of Rutford Ice Stream. Additionally, within the same ice stream, Smith et al. (2017) showed that a combination of vertical and horizontal c-axis alignment, termed a "horizontal partial girdle," leads to enhanced horizontal shearing in a vertical plane aligned with the ice flow direction.

Here, we build upon the previous characterization of ice fabric and its impact on ice viscosity within Rutford Ice Stream using polarimetric radar sounding. This technique is sensitive to crystallographic-preferred orientation in the horizontal plane, perpendicular to the radar propagation direction, which we will refer to as "azimuthal fabric anisotropy." Specifically, we characterize how azimuthal fabric orientation and strength vary spatially within the near surface of the ice stream (top 300 m) and compare with the ice-surface strain field. The fabric estimation uses a recently developed polarimetric coherence (phase-based) method (Dall, 2010; Jordan et al., 2019; Jordan, Schroeder, et al., 2020; Young, Martín, et al., 2021). This method exploits principles analogous to radar interferometry using the polarimetric phase difference to place precise constraints on the azimuthal fabric orientation and azimuthal strength. Radar fabric estimates have typically been used to investigate ice-flow history (Brisbourne et al., 2019; Fujita et al., 2006; K. Matsuoka et al., 2012), but have not been used to constrain anisotropic viscosity. To address this deficiency, we develop a new framework where radar fabric measurements are used to parameterize a tensorial anisotropic flow law (Gillet-Chaulet et al., 2005; Godert, 2003; Martin et al., 2009) and thereby constrain the anisotropic viscosity of ice.

This paper is organized as follows. In Section 2, we describe the survey region, data acquisition, and computation of the ice-surface strain field. In Section 3, we outline the tensor representation of ice fabric and show how polarimetric radar measurements of azimuthal anisotropy can be used to bound fabric in both horizontal and vertical directions. In Section 4, we present the polarimetric coherence method used to estimate the fabric, detailing ongoing improvements to the technique. In Section 5, we show how the radar measurements can be used to constrain effective anisotropic viscosities of ice (directional hardening). In Section 6, we present results for

Table 1
Glossary of Key Symbols

Category	Symbol	Description
Ice motion	$\mathbf{D}$	3×3 strain-rate tensor
	$\bar{\boldsymbol{S}}$	3×3 deviatoric stress tensor
	θ_t	Azimuthal angle tangential to ice flow in stereographic coordinates
	θ_{min}	Azimuthal angle of principal compression in stereographic coordinates
Fabric	$\mathbf{a}$	3×3 second order orientation tensor
	$a_y - a_x$	Azimuthal strength of fabric measured by radar
	θ_y	Azimuthal angle of fabric (greatest horizontal c-axis alignment)
Rheology	$\boldsymbol{\eta}$	6×6 matrix representation of fourth-order viscosity tensor
Radar analysis	S	2×2 scattering matrix
	c_{hhvv}	*hhvv* (polarimetric) coherence
	ϕ_{hhvv}	*hhvv* coherence phase (co-polarized phase difference)
	$\Delta\epsilon'$	Ice crystal birefringence
	$\bar{\epsilon}$	Mean (polarization averaged) permittivity
	H, V	Polarizations in quad-polarized (fixed) basis
	h, v	Polarizations in multi-polarized (rotating) basis
Coordinate systems	$\mathbf{x}_1$, $\mathbf{x}_2$, $\mathbf{x}_3$	Principal axes of $\mathbf{a}$ and $\boldsymbol{\eta}$: $a_3 > a_2 > a_1$
	$\mathbf{x}$, $\mathbf{y}$, $\mathbf{z}$	Principal axes of $\mathbf{a}$ and $\boldsymbol{\eta}$ referenced to ice sheet: $\mathbf{x}$ and $\mathbf{y}$ horizontal with $a_y > a_x$ and $\mathbf{z}$ vertical
	z	Scalar ice depth coordinate
	$\mathbf{t}$, $\mathbf{n}$	Local ice-flow coordinate axes ($\mathbf{t}$: tangential to flow, $\mathbf{n}$: normal to flow)
	$\mathbf{x}_{min}$, $\mathbf{x}_{max}$	Horizontal principal axes of $\mathbf{D}$ ($\mathbf{x}_{min}$: compression, $\mathbf{x}_{max}$: extension)

spatial development in ice fabric and associated directional hardening of ice to uniaxial strain and lateral shear within the Rutford Ice Stream. In Section 7, we discuss the implications of the study. A summary of the key parameters used in the study is provided in Table 1.

2. Survey Region, Data Acquisition, and Calculating Ice-Surface Strain

2.1. Survey Region

Rutford Ice Stream, West Antarctica, flows approximately southward into the Filchner-Ronne Ice Shelf and is bounded by the Fletcher Promontory and Ellsworth Mountains to the east and west, respectively (Figure 1a). The survey region (Figures 1b and 1c) is located between 40 and 80 km upstream of the grounding line where the ice stream is approximately 25 km wide with ice-flow speed approximately 340 m a^{-1} (Rignot et al., 2011, 2017). The ice thickness within the survey region is approximately 2.2 km (E. C. King et al., 2016).

The ground-based radar survey consists of 20 discrete measurement sites along two separate transects. Transect A, collected on 20 January 2017, is orientated perpendicular to the ice flow direction. It consists of 10 sites (labeled A1–A10 from west to east) between the center streamline and the ice-stream margin and is of total length 8.5 km with the inter-site spacing decreasing toward the ice-stream margin. Transect B, collected on 5 December 2019, is orientated parallel to the central flow line. It consists of 10 sites (labeled B1–B10 from south to north) with the first site 4 km upstream of site A1 and the inter-site distance spacing fixed at 4 km.

2.2. Polarimetric Data Acquisition

At each survey site, polarimetric radar-sounding measurements were made using an autonomous phase-sensitive radio-echo sounder (ApRES), a frequency-modulated continuous-wave radar. The ApRES has a center frequency

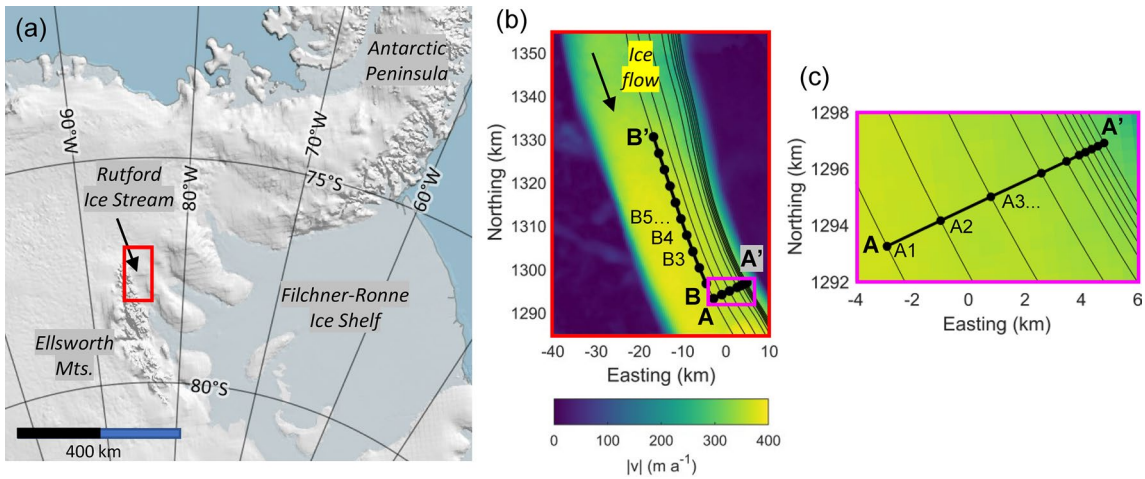

Figure 1. Glaciological setting and radar measurement sites. (a) Location of Rutford Ice Stream and the survey region (red box). (b) Survey transects (thick black lines), measurement sites (black circles), and ice-flow streamlines (thin black lines) underlain by ice surface speed, |v|. (c) Zoom to Transect A (indicated by pink box in (b)). The maps in (b) and (c) were generated using Antarctic Mapping Tools (Greene et al., 2017) and assume a reference meridian 83.8°W.

of 300 MHz and a bandwidth of 200 MHz, which results in a range resolution of approximately 40 cm in ice. Further radar system details are provided by Brennan et al. (2014) and Nicholls et al. (2015).

The material anisotropy in the horizontal plane, perpendicular to vertical propagation of the radio wave, is determined from the differences in the returns from four sets of transmit and receive antenna orientations. These are referred to as "quad-polarized" acquisitions and are obtained by sequentially rotating the transmit and receive antennas (horizontally separated by ≈8 m) by 90°. We notate the quad-polarized measurements in an *HV* basis, where *H* and *V* notate that the polarization plane is parallel to true west/east and north/south, respectively. Data were acquired with the antenna oriented with respect to magnetic north and subsequently corrected to geographic coordinates by applying a declination of 40°E (assumed constant for the survey).

To range process the raw data, we follow Brennan et al. (2014) and obtain a set of four complex amplitudes s_{HH}, s_{VH}, s_{HV}, s_{VH}, where the first and second subscripts indicate the transmit and receive polarization states, respectively. The complex amplitudes constitute the scattering matrix, $S_{HV} = [s_{HH}, s_{HV}; s_{VH}, s_{VV}]$, which relate the phase and magnitude of the transmitted and received electric field for each polarization state (Boerner, 1992; Doake et al., 2003).

2.3. Calculating the Ice-Surface Strain Field

Of interest in this study is the relationship between the horizontal part of the ice-surface strain-rate tensor, **D**, and the fabric and viscosity estimates (also formulated as the horizontal part of their respective tensors). In the data analysis, we express **D** in the principal coordinate system (the maximum and minimum strain axes, $\mathbf{x}_{max}$ and $\mathbf{x}_{min}$) and a local ice-flow coordinate system (**t** axis tangential and **n** axis normal to ice flow). The principal coordinates are most appropriate to understand fabric development, and the ice-flow coordinates are most appropriate to understand the effects of anisotropic viscosity on ice deformation.

D was initially computed in polar stereographic coordinates by differentiating horizontal ice-surface velocity components from the MEaSUREs data product (Rignot et al., 2011, 2017), which is supplied at an approximately 440 m grid resolution. The velocity-derivative procedure follows Jordan, Schroeder, et al. (2020) and uses a convolution derivative with Gaussian kernel and standard deviation ≈ 1.8 km. The principal strain rates, D_{max} and D_{min}, corresponding to the strain along $\mathbf{x}_{max}$ and $\mathbf{x}_{min}$, were then obtained by solving the eigenvalue problem. The strain rates in the ice-flow coordinates, D_{tt} (uniaxial strain tangential to flow), D_{nn} (uniaxial strain normal to flow), and D_{tn} (lateral shear in the ice-flow coordinates) were obtained via an azimuthal rotation transform of **D**.

The strain-rate uncertainty was estimated via the propagation of the standard error on velocity components (Rignot et al., 2011, 2017). This was done numerically by generating an ensemble of velocities normally distributed

within their provided uncertainty and then computing spatial velocity derivatives. The strain-rate estimates and their uncertainty were then derived from the mean and standard deviation of the velocity-derivative ensemble.

3. Representation of Ice Crystal Orientation Fabrics

3.1. The Second-Order Orientation Tensor

Following previous polarimetric radar-sounding studies (e.g., Fujita et al. (2006); K. Matsuoka et al. (2012); Brisbourne et al. (2019); Jordan et al. (2019)), we model the *c*-axis orientation distribution using the second-order orientation tensor, **a** (Woodcock, 1977). The tensor eigenvalues, a_1, a_2, and a_3 represent the relative *c*-axis concentration along each principal coordinate direction $\mathbf{x}_1$, $\mathbf{x}_2$, $\mathbf{x}_3$ (from herein referred to as "fabric eigenvalues" and "fabric eigenvectors"). Geometrically, the eigenvalues are the axes length of an ellipsoid that best fits the grain orientation distribution (Montagnat et al., 2014). The fabric eigenvalues have the properties $a_1 + a_2 + a_3 = 1$, and $a_3 > a_2 > a_1$. The principal coordinates correspond to a base system where the orientation tensor is diagonal and therefore easier to interpret and are generally not aligned with ice flow.

The second-order orientation tensor is a simplified representation of the fabric that, in general, can be represented as an expansion of even-order orientation tensors (Gillet-Chaulet et al., 2005). Only the second-order orientation tensor can be measured by radar as the dielectric tensor, which represents the material anisotropy experienced by the radio wave and maps to the orientation tensor, is second order (Fujita et al., 2006; Hargreaves, 1978). This means that higher-order features (e.g., multiple poles) cannot be discriminated. Under the second-order tensor representation, ice fabrics can be categorized using the following end-members: "random/isotropic" $\left(a_1 \approx a_2 \approx a_3 \approx \frac{1}{3}\right)$, "single-pole" ($a_1 \approx a_2 \approx 0$, $a_3 \approx 1$) and "girdle" $\left(a_1 \approx 0, a_2 \approx a_3 \approx \frac{1}{2}\right)$.

3.2. Assumptions About Fabric Orientation Within Radar Sounding

In downward-looking radar sounding (with antenna approximately colocated), the radio wave polarizations are parallel to the ice surface. Consequently, as the polarizations are sensitive to material properties in the direction which they oscillate, the technique detects fabric anisotropy, at a given depth, in a horizontal plane parallel to the ice surface, which we will refer to as "azimuthal fabric anisotropy." The retrieval of azimuthal fabric anisotropy from the polarimetric backscatter model (Fujita et al., 2006; Jordan et al., 2019) makes the assumption that one of the fabric eigenvectors is aligned with the vertical. Under this assumption, the radar is used to estimate the azimuthal orientation of the horizontal eigenvectors and the horizontal eigenvalue difference (often referred to as "azimuthal strength" or "asymmetry"). Modeling radio propagation where one of the fabric eigenvectors is not aligned with the vertical is considerably more complex (Jordan, Besson, et al., 2020; K. Matsuoka et al., 2009) and is not considered in this study. Rathmann et al. (2022) demonstrate that vertical incidence radar measurements are insensitive to a non-vertical principal axis direction and highlight the need for oblique measurements to constrain the full second-order structure tensor, requiring wide-angle radar measurements that are not available in this study.

Previous radar-sounding studies have assumed that the $\mathbf{x}_3$ axis (direction of greatest c-axis alignment) is vertical with the $\mathbf{x}_1$ and $\mathbf{x}_2$ axes in the horizontal plane (e.g., Fujita et al. (2006); K. Matsuoka et al. (2012); Brisbourne et al. (2019); Jordan et al. (2019)). This assumption is likely to be valid in slow-flow regions, such as ice divides and domes, where vertical compression is the dominant stress component, and also within the trunk of an ice stream (Lilien et al., 2021). In parts of fast-flowing ice-streams where horizontal stresses are dominant, that is toward the shear margins, the fabric is consistent with either the $\mathbf{x}_1$ or $\mathbf{x}_2$ axis being approximated as vertical (Lilien et al., 2021). We note that a previous study utilizing seismic shear-wave splitting over central Rutford Ice Stream (Smith et al., 2017) indicated a column-averaged bulk fabric with $\mathbf{x}_3$ horizontal.

In this study, we consider three model permutations of the principal axis relative to the ice-sheet coordinates, which we refer to as "$\mathbf{x}_3$ vertical" ($\mathbf{x}_2$ and $\mathbf{x}_1$ horizontal), "$\mathbf{x}_2$ vertical" ($\mathbf{x}_3$ and $\mathbf{x}_1$ horizontal), and "$\mathbf{x}_1$ vertical" ($\mathbf{x}_2$ and $\mathbf{x}_3$ horizontal). These permutations represent end-members for the orientation of **a** that can be interpreted in the radar analysis. To simplify the notation, all three model permutations use **x** and **y** to notate the horizontal eigenvectors and **z** to notate the vertical eigenvector with the corresponding fabric eigenvalues a_x, a_y, and a_z, respectively. The convention $a_y > a_x$ is assumed and therefore **y** represents the direction of greatest

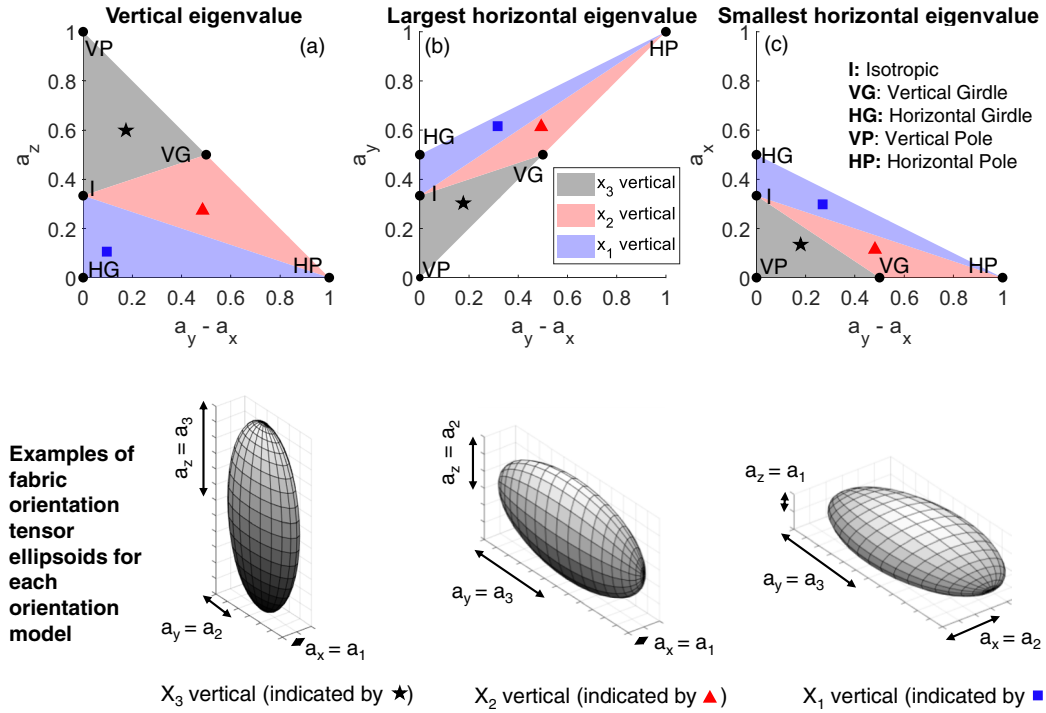

Figure 2. Bounding fabric eigenvalues from the radar measurement of the horizontal eigenvalue difference, a_y - a_x. (a) Vertical eigenvalue. (b) Largest horizontal eigenvalue. (c) Smallest horizontal eigenvalue. Eigenvalues consistent with the bounds for each principal orientation model are indicated by the different colors. Visual examples of the fabric orientation tensor ellipsoid are shown in the bottom row and are indicated in the eigenvalue plots. The limiting fabric states are indicated by black circles in each subplot.

horizontal c-axis alignment. The horizontal eigenvalue difference measured by the radar is interpreted as either: $a_y - a_x = a_2 - a_1$ ($\mathbf{x}_3$ vertical), $a_y - a_x = a_3 - a_1$ ($\mathbf{x}_2$ vertical), and $a_y - a_x = a_3 - a_2$ ($\mathbf{x}_1$ vertical).

3.3. Bounding Three-Dimensional Fabric From Radar Sounding

To parameterize the anisotropic flow-law (viscosity tensor) knowledge of all three fabric eigenvalues is required. Within each principal orientation model, the constraints $a_3 > a_2 > a_1 > 0$ and $a_3 + a_2 + a_1 = 1$ enable bounds on possible values of a_z, a_y, and a_x for each measured value of $a_y - a_x$ to be derived. The model bounds for each eigenvalue are shown by the shaded regions in Figure 2 with limiting fabric states indicated (Isotropic (I): $a_z = a_y = a_x = \frac{1}{3}$, Vertical girdle (VG): $a_z = a_y = \frac{1}{2}$, $a_x = 0$, Vertical pole (VP): $a_z = 1$, $a_y = a_x = 0$, Horizontal girdle (HG): $a_z = 0$, $a_y = a_x = \frac{1}{2}$, and Horizontal pole (HP): $a_z = a_x = 0$, $a_y = 1$). Visual examples of the orientation tensor ellipsoid are also included. The eigenvalue bounds on each orientation model can be interpreted as maximizing or minimizing the vertical eigenvalue (a_z) as shown in Figure 2a and are used to calculate corresponding bounds on the viscosity tensor elements in Section 5.

The fabric eigenvalues are better constrained as a_y - a_x increases (in particular, the limiting case of a horizontal pole when a_y - $a_x = 1$). In this study, and to the best of our knowledge, all previous radar fabric studies, the measured values of $a_y - a_x$ are always less than 0.5. However, the region $a_y - a_x > 0.5$ is included in Figure 2 for completeness if future studies may measure greater values of $a_y - a_x$.

4. Polarimetric Data Analysis

4.1. Overview of the Polarimetric Coherence Method

The procedure to estimate ice fabric from the polarimetric radar data is based on a previously developed polarimetric coherence method (Dall, 2009; 2010; Jordan et al., 2019; Jordan, Schroeder, et al., 2020; Young, Martín,

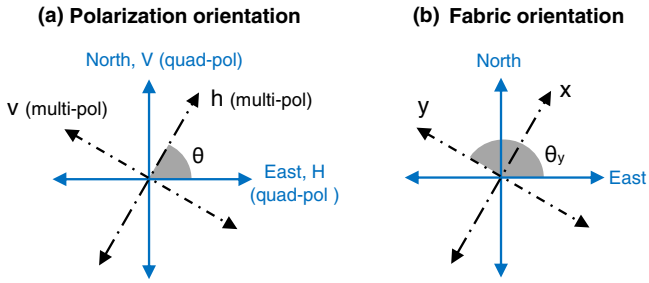

Figure 3. (a) Orientation convention for radar polarization planes in quad- (HV) and multi-polarized (hv) bases. The data analysis is performed in stereographic coordinates by applying a prior magnetic declination correction of 40°E. The azimuthal angle, θ, is by convention measured positive in a counterclockwise direction from true east. (b) Orientation convention for horizontal fabric eigenvectors, where **y** and **x** represent the direction of greatest and least horizontal c-axis alignment, respectively, with θ_y and $\theta_x = \theta_y - 90°$ the corresponding azimuthal angles.

et al., 2021). The method exploits the fact that azimuthal fabric anisotropy results in a bulk ice birefringence; a dielectric material property that results in the radio wave phase velocity being a function of polarization. The term "polarimetric coherence" refers to a phase-correlation method that is then used to measure the polarimetric phase difference. The measured form of the polarimetric phase difference, the *hhvv* coherence phase (ϕ_{hhvv}), is analogous to the interferometric phase in radar interferometry, but relates to material anisotropy due to the fabric rather than a physical displacement. The polarimetric coherence method reduces ambiguities that are introduced when using radar power to estimate ice fabric and better enables measurement uncertainty to be incorporated (Jordan et al., 2019; Jordan, Schroeder, et al., 2020).

In Section 4.2, we outline the key principles in the coherence data analysis. In Section 4.3, we describe new method development that improves automation of the fabric estimates from previous studies (Jordan et al., 2019; Jordan, Schroeder, et al., 2020). The coherence method is underpinned by a polarimetric backscatter model of the ice sheet, which relates the ice fabric parameters to the measured scattering matrix and derived quantities (Fujita et al., 2006; Jordan et al., 2019). A reader requiring a full electromagnetic treatment of the backscatter model is referred to Fujita et al. (2006). A reader requiring a presentation of how the coherence methodology relates to the backscatter model is referred to Jordan et al. (2019), adaptation to quad-pol data described by Young, Martín, et al. (2021), and initial proof-of-concept of the technique by Dall (2009); Dall (2010).

4.2. Polarimetric Coherence: Key Principles

The polarimetric coherence analysis is formulated in a "multi-polarization plane" basis (co-polarized complex amplitude data as a function of azimuthal angle). Following Jordan et al. (2019), the multi-polarization data are notated by h and v where the orientation of h and v is a function of the bearing angle θ, measured in a counterclockwise direction from true east (Figure 3a). When $\theta = 0°$ and 180°, h is aligned with H (true east/west) and v is aligned with V (true north/south). To generate the multi-polarization data from the quad-polarized acquisition, a rotation basis transformation was applied to the scattering matrix (Young, Martín, et al., 2021) and validated by checking for conserved quantities (Boerner, 1992). Due to the use of the rotation transformation, the set of quad-pol measurements can be made with respect to any reference azimuth. The technique is generally limited by the power signal-to-noise-ratio (SNR) of HV and VH terms as these have lower power SNR than the HH and VV terms. In this study, we always have sufficiently high SNR as we focus on shallower ice. The azimuthal angle of the fabric is referenced to the polarizations in Figure 3b where θ_y is defined as the angle of greatest horizontal c-axis alignment.

The polarimetric (*hhvv*) coherence is calculated as a function of azimuthal angle and ice depth, z, by windowing data in the range direction using

$$c_{hhvv}(\theta, z) = \frac{\sum_{j=1}^{N} s_{hh,j} . s^{*}_{vv,j}}{\sqrt{\sum_{j=1}^{N} |s_{hh,j}|^2} \sqrt{\sum_{j=1}^{N} |s_{vv,j}|^2}}, \quad (1)$$

where j is the range bin index and represents a depth, N is the number of independent range pixels, and * indicates complex conjugate. In the data analysis, we assume a sliding range window of 40 m, corresponding to $N = 96$ (refer to the, Figures S7 and S8 in Supporting Information S1, for sensitivity experiments). c_{hhvv} is a complex number where the magnitude, $|c_{hhvv}|$, describes the correlation between s_{hh} and s_{vv} and ranges from zero to unity. $|c_{hhvv}|$ is impacted by the power SNR and is higher when there are flat and ordered radar layers present in the ice sheet, such as at ice divides (Jordan et al., 2019) or ice domes (Ershadi et al., 2021). The complex argument,

$$\arg(c_{hhvv}) = \phi_{hhvv} = \phi_{hh} - \phi_{vv}, \quad (2)$$

referred to as the *hhvv* coherence phase, defines the relative polarimetric phase shift between co-polarized acquisitions that are offset by 90° azimuth to each other. The Cramer-Rao bound (Touzi & Lopes, 1999) can be used to estimate the phase error from $|c_{hhvv}|$ via

$$\sigma_{\phi_{hhvv}} \approx \frac{1}{|c_{hhvv}|}\sqrt{\frac{1-|c_{hhvv}|^2}{2N}}. \tag{3}$$

The central equation that connects ϕ_{hhvv} to the ice fabric is given by

$$\left(\frac{d\phi_{hhvv}}{dz}\right)_{\theta=\theta_x,\theta_y} = \pm\frac{4\pi f_c}{c}\frac{\Delta\epsilon'(a_y-a_x)}{\sqrt{2\bar{\epsilon}}}, \tag{4}$$

where f_c is the radar center frequency, c is the radio wave speed, $\bar{\epsilon}$ is the mean (polarization averaged) permittivity, $\Delta\epsilon' = (\epsilon_{\parallel c} - \epsilon_{\perp c})$ is the birefringence of an ice crystal with $\epsilon_{\parallel c}$ and $\epsilon_{\perp c}$ the permittivity parallel and perpendicular to the c axis, respectively. As described in Section 3, the horizontal eigenvalue difference, $a_y - a_x$, can be interpreted as either $a_2 - a_1$ ($\mathbf{x}_3$ assumed vertical), $a_3 - a_2$ ($\mathbf{x}_2$ assumed vertical), or $a_3 - a_1$ ($\mathbf{x}_1$ assumed vertical). The temperature and frequency dependence of the ice permittivity is summarized by Fujita et al. (2000), T. Matsuoka et al. (1996), and Fujita et al. (2006). Here, we assume commonly used values within radar-sounding of $\Delta\epsilon' = 0.034$ and $\bar{\epsilon} = 3.15$. A negative phase gradient, $\frac{d\phi_{hhvv}}{dz} < 0$, occurs when $\theta = \theta_y$ as the h polarization is aligned with a higher permittivity than the v polarization and therefore has a lower phase velocity. In turn, the higher permittivity is associated with a greater azimuthal c-axis alignment. In the data analysis, $\frac{d\phi_{hhvv}}{dz}$ was computed using a convolution derivative (analogous to the surface strain derivative in Section 2.3) with the Gaussian kernel standard deviation size matching the coherence bin size.

Following Jordan, Schroeder, et al. (2020), we take into account the effects of phase de-ramping in the ApRES processing (Brennan et al., 2014) by taking the complex conjugate of c_{hhvv}, but do not notate this explicitly in the data analysis.

4.3. Automated Extraction of Ice Fabric

To demonstrate how the fabric estimation is automated, we input synthetic data (depth profiles for $\theta_y(z)$ and $(a_y - a_x)(z)$) into the polarimetric backscatter model (Fujita et al., 2006; Jordan et al., 2019) and compare with the retrieved fabric estimates. In the fitting, we incorporate two sources of uncertainty. First, we incorporate uncertainty in the antenna/polarization plane alignment by assuming an alignment uncertainty of ±5° for each *HV* acquisition pair. Second, we incorporate uncertainty due to phase decoherence ($|c_{hvvv}| < 1$) by evaluating Equation 3 for measured values of $|c_{hvvv}|$. Further details of how this uncertainty is propagated within the processing chain are given in the Supporting Information (Figure S1 in Supporting Information S1).

We illustrate the approach using three examples of increasing complexity. In the synthetic examples, $|c_{hvvv}|$ is modeled using a linearly decreasing ramp function with ice depth, which approximates the decoherence of the ice-stream data in Section 6.2. The first example (Figure 4a) considers a depth-invariant fabric orientation but increasing azimuthal fabric strength with depth. The second example (Figure 4b) considers 90° azimuthal rotation within the ice column. The third example (Figure 4c) considers a gradual (non-90°) azimuthal fabric rotation with depth. Estimation of fabrics that approximate Case 1 has been validated using ice core fabric data and comparative analyses between different radar systems (Dall, 2010; Jordan et al., 2019; Li et al., 2018).

The fabric estimation procedure first solves for $\theta_y(z)$ then $(a_y - a_x)(z)$. To fit for $\theta_y(z)$, we exploit the fact that $\frac{d\phi_{hhvv}}{dz}$ has either exact (Figures 4a and 4b) or approximate (Figure 4c) the azimuthal reflection symmetry about θ_y. To implement the constraint and solve for $\theta_y(z)$ numerically, we minimized a cost function at each depth (see Section 1 in Supporting Information S1). Once $\theta_y(z)$ is established, $(a_y - a_x)(z)$ is obtained by substituting $\left|\left(\frac{d\phi_{hhvv}}{dz}\right)_{\theta=\theta_y}\right|$ into Equation 4 and rearranging.

The examples in Figures 4a and 4b illustrate agreement between the true (synthetic) and retrieved (fitted) values of θ_y. In the deeper ice, the accuracy of the estimates decreases with $|c_{hhvv}|$ due to the related coherence phase error, Equation 3. Additionally, at the depth when θ_y rotates by 90° in Figure 4b, the estimates for $(a_y - a_x)(z)$ are impacted by the assumed 40-m window size. The third example illustrates that non-90° rotations can result

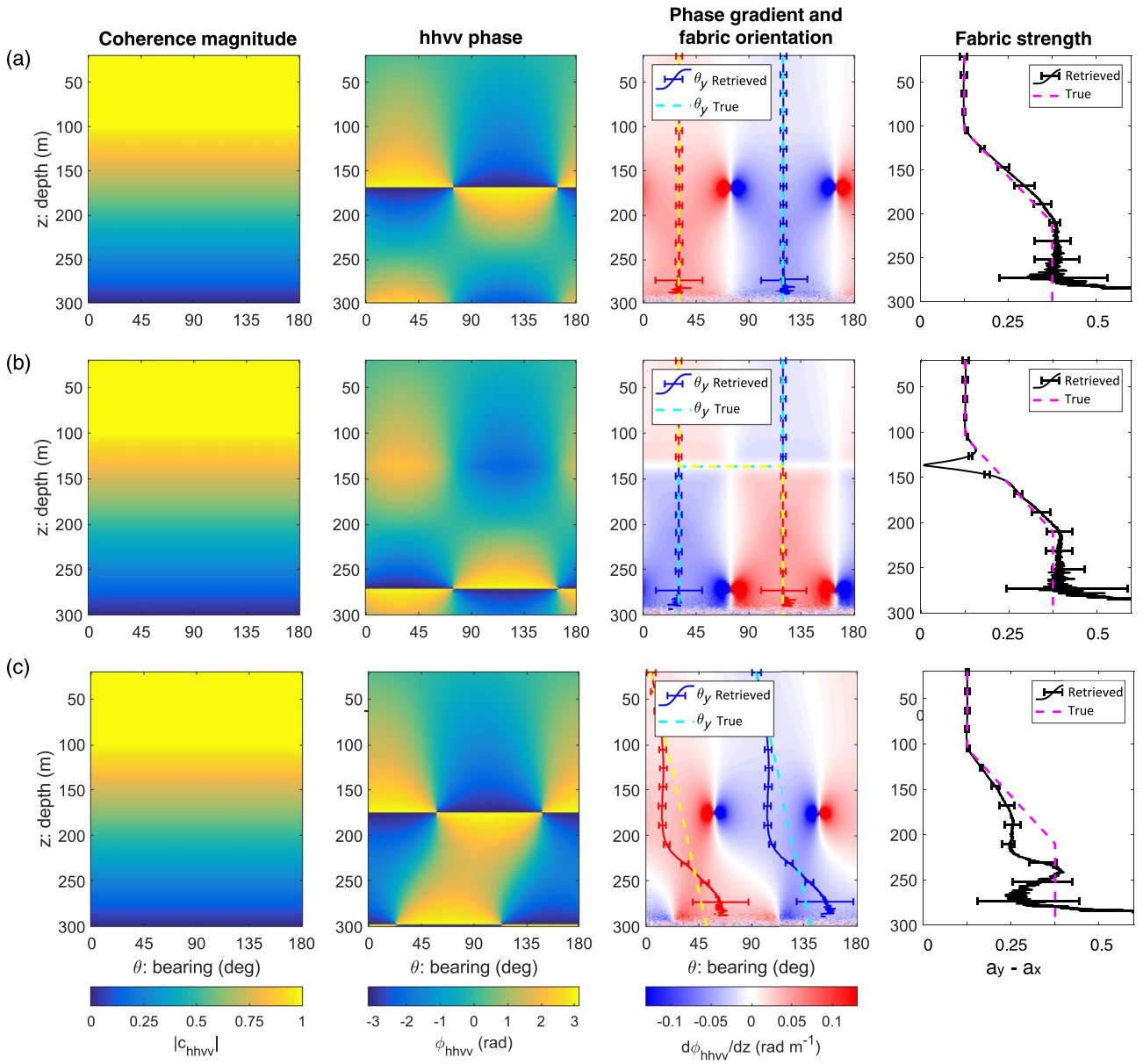

Figure 4. Illustration of fabric estimation using the polarimetric backscatter model with synthetic data. (a) Case 1: Depth-invariant fabric orientation. (b) Case 2: Sharp (90°) azimuthal rotation. (c) Case 3: Gradual azimuthal rotation. In the plot legends, "True value" refers to input synthetic fabric data and "Retrieved value" refers to fabric estimates using a symmetry constraint (see Section 1 in Supporting Information S1). θ_y corresponds to the azimuthal angle of the **y** axis (angle of greatest horizontal c-axis alignment). The true and retrieved values for θ_x (angle of least horizontal c-axis alignment) are indicated by the dashed yellow and solid red lines, respectively.

in biases in the data fits. The sense of rotation is, however, correctly accounted for. The examples show that the fits for $(a_y - a_x)(z)$ are generally less robust than θ_y in the presence of phase decoherence. In the data analysis, Section 6.2, we demonstrate that the fabric is well-approximated by the first and second examples, and example 3 is intended to guide method development that may be required in future studies.

The backscatter model simulations in Figure 4 all assume isotropic specular reflection from the englacial layers. However, due to preserved azimuthal symmetry properties (Jordan et al., 2019), the fitting approach also generalizes to anisotropic reflectors. Isotropic reflection encompasses reflection from conductivity, density, and some classes of fabric reflectors, whereas anisotropic specular reflection arises purely from fabric reflectors (Fujita et al., 1999).

5. Radar Characterization of Anisotropic Ice Viscosity

5.1. Overview of Anisotropic Flow Law and Viscosity Tensor

The aim of this section is to provide a scheme to input the radar fabric measurements into an anisotropic flow law using the GOLF (general linear orthotropic flow law) model (Castelnau et al., 1996; Gillet-Chaulet et al., 2005, 2006). This model is formulated in terms of the effective viscosity tensor, which quantifies how the fabric results in directional hardening of ice for different stress components. The ice is assumed to behave as a linearly viscous orthotropic material, a class of anisotropic material where the mechanical properties are symmetrical with respect to three orthogonal planes (Gagliardini & Meyssonnier, 1999; Gillet-Chaulet et al., 2005; Martin et al., 2009). The new contribution here is to consider how the azimuthal cross section of the fabric that is measured by the radar, expressed as an azimuthal orientation relative to ice flow, $\theta_y - \theta_t$, and azimuthal strength, $a_y - a_x$, bound the effective viscosity tensor elements (following the eigenvalue bounds in Figure 2). For completeness, we consider a full range of possible fabric states that can be measured by the radar, which extends beyond the data set in this paper.

We follow the presentation of the flow law in the appendix of Martin et al. (2009), based on Gillet-Chaulet et al. (2005) and Gagliardini and Meyssonnier (1999). In the orthotropic reference frame the strain, $\mathbf{D}$, and deviatoric stress, $\bar{\boldsymbol{S}}$, tensors can be written as 6-component vectors, which are connected via the matrix equation

$$\begin{pmatrix} \bar{S}_{xx} \\ \bar{S}_{yy} \\ \bar{S}_{zz} \\ \bar{S}_{xy} \\ \bar{S}_{xz} \\ \bar{S}_{yz} \end{pmatrix} = \eta_0 \begin{pmatrix} \eta_{xxxx} & \eta_{xxyy} & \eta_{xxzz} & 0 & 0 & 0 \\ \eta_{xxyy} & \eta_{yyyy} & \eta_{yyzz} & 0 & 0 & 0 \\ \eta_{xxzz} & \eta_{yyzz} & \eta_{zzzz} & 0 & 0 & 0 \\ 0 & 0 & 0 & \eta_{xyxy} & 0 & 0 \\ 0 & 0 & 0 & 0 & \eta_{xzxz} & 0 \\ 0 & 0 & 0 & 0 & 0 & \eta_{yzyz} \end{pmatrix} \begin{pmatrix} D_{xx} \\ D_{yy} \\ D_{zz} \\ D_{xy} \\ D_{xz} \\ D_{yz} \end{pmatrix}, \tag{5}$$

where $\boldsymbol{\eta}$ is the matrix representation of the fourth-order effective viscosity tensor and η_0 is a constant. The elements of $\boldsymbol{\eta}$ represent the relative hardness of each deformation mode with respect to an isotropic fabric, whereby values greater than one indicate anisotropic ice that is harder than isotropic ice to an applied stress component. In this study, we focus on constraining η_{xxxx}, η_{yyyy}, and η_{xyxy} with the radar method as these are the viscosity components that can best be related to the surface strain rates. η_{xxxx} and η_{yyyy} represent the directional hardness of ice to uniaxial strain (compression or extension) along the **x** and **y** axes (directions of least and greatest horizontal c-axis alignment) and η_{xyxy} represents the hardness to lateral shear. For convenience, we sometimes refer to effective viscosity as viscosity.

Anisotropy in the effective viscosity arises due to a combination of mechanical anisotropy at a crystal scale (assumed model parameters) and how the grain-scale anisotropy translates to a larger-scale fabric (radar measurements). The crystal-scale anisotropy is parameterized via two ratios: (a) "the viscosity of the grain for shear parallel to the basal plane to that in the basal plane," β, and (b) "the ratio of the viscosity in compression or tension along the c-axis to that in the basal plane," γ. To estimate the effective viscosity tensor η, we use the GOLF model (Castelnau et al., 1996; Gillet-Chaulet et al., 2005, 2006) as provided by the AIFlow Solver within ElmerIce (Gagliardini et al., 2013). The model searches a parameter space for a given second-order orientation tensor, **a**, that has been tabulated using different viscosity models and crystal-scale parameters. In this paper, we assume that $\beta = 0.04$, $\gamma = 1$, and that the model used for tabulation is a viscoplastic self-consistent model.

The viscosity elements in the principal coordinates (Equation 5) serve as bounding cases but can be better related to ice dynamics in the ice-flow coordinates: **t** (tangential/along-flow) and **n** (normal/across-flow). In the AIFlow Solver, the rotation transform applies to the input **a** tensor (estimated from radar following the bounds in Figure 2) and uses a standard two-dimensional rotation matrix. The rotation angle is defined such that when $\theta_y - \theta_t = 0°$ **y** is aligned with **t** (i.e., the fabric is aligned with ice flow).

A nonlinear extension of Equation 5 is considered by Martin et al. (2009) and Ma et al. (2010), which mimics the third-power dependence of the commonly used Glen's flow-law (Glen, 1954). Consequently, while we focus on a

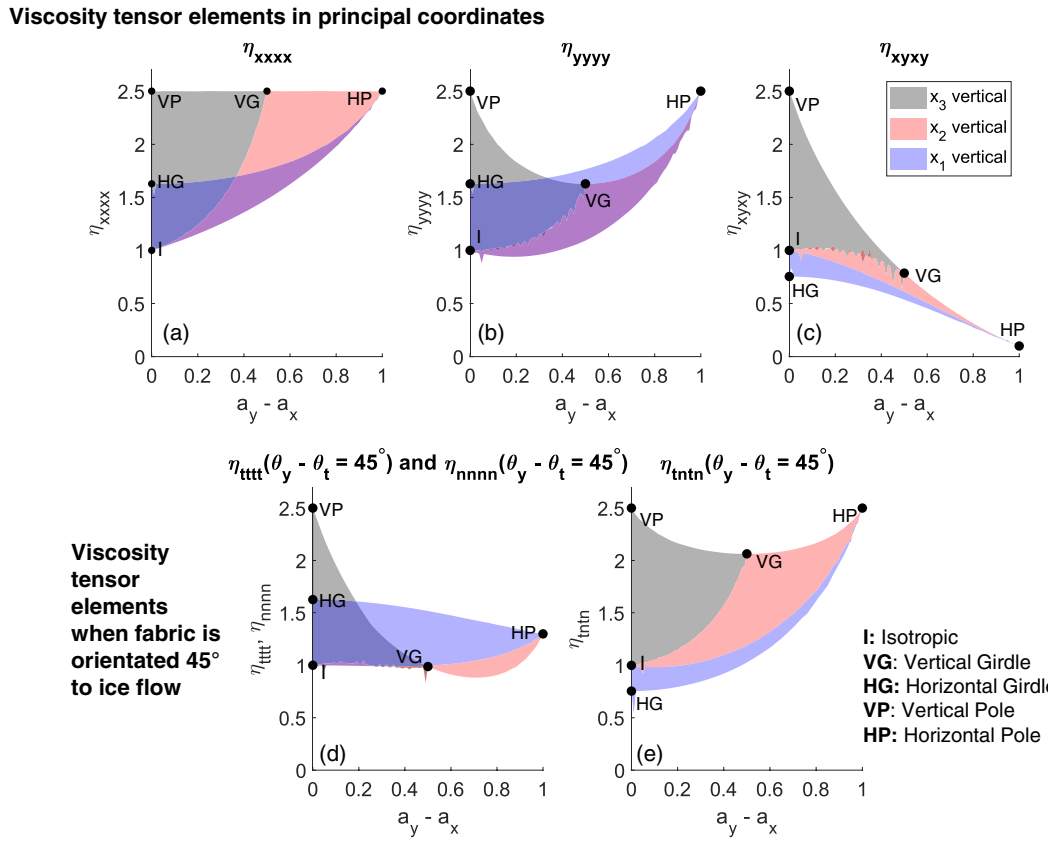

Figure 5. Bounds on the horizontal elements of viscosity tensor that follow from radar measurement of a_y - a_x. Top row (principal coordinates): (a) η_{xxxx} (equivalent to η_{nnnn} when θ_y - $\theta_t = 0°$), (b) η_{yyyy} (equivalent to η_{tttt} when θ_y - $\theta_t = 0°$), and (c) η_{xyxy} (equivalent to η_{tntn} when θ_y - $\theta_t = 0°$). Bottom row (fabric orientated at 45° to ice flow): (d) η_{tttt} ($\theta_y - \theta_t = 45°$) = η_{nnnn} ($\theta_y - \theta_t = 45°$) and (e) η_{tntn} ($\theta_y - \theta_t = 45°$). Viscosity values greater or less than one indicate that anisotropic ice is harder or softer than isotropic ice, respectively. An overlap between end-member orientation models occurs in panels (a), (b), and (d).

linear anisotropic viscosity in this study, the radar measurements could also be used to parameterize a nonlinear anisotropic flow law.

5.2. Bounding the Effective Viscosity Tensor Elements From the Radar Fabric Measurements

We focus on illustrating how radar can constrain the horizontal viscosity tensor elements as these can best be compared with the horizontal ice-surface strain rates. We first show results in the principal coordinates (top row of Figure 5). As is the case for the fabric eigenvalues (Figure 2), the viscosity tensor elements are better constrained with increasing a_y - a_x. The limiting fabric states are indicated in Figure 2 and we now discuss these cases using the terminology "hard" and "soft" for effective viscosity elements greater or less than one, which is the viscosity for isotropic ice (I). A vertical pole (VP) fabric results in ice being equally hard to the horizontal uniaxial strain in the **x** and **y** directions and to lateral shear. A vertical girdle (VG) fabric results in ice being hard to the uniaxial strain in the **x** and **y** directions with the ice hardest in the **x** direction. A vertical girdle (VG) fabric also results in ice being slightly soft to lateral shear. A horizontal pole (HP) fabric results in ice being equally hard to the uniaxial strain in both **x** and **y** directions but very soft to lateral shear. A horizontal girdle (HG) fabric results in ice being equally hard to the uniaxial strain in both the **x** and **y** directions but slightly soft to lateral shear. Similar constraints to Figure 5 can also be obtained on η_{xzxz}, η_{zzzz}, and η_{yzyz}. We did not consider these viscosity components as they are less directly comparable with the surface strain rates.

We later show that the ice fabric near the margin of Rutford Ice Stream tends toward 45° relative to ice flow. To contextualize this result, viscosity elements in the ice-flow coordinates when $\theta_y - \theta_t = 45°$ are shown in the bottom row of Figure 5. By symmetry, when $\theta_y - \theta_t = 45°$ $\eta_{tttt} = \eta_{nnnn}$, and the ice is generally softer to uniaxial

strain than in the principal coordinates. However, when $\theta_y - \theta_t = 45°$, ice generally becomes harder to lateral shear than in the principal coordinates. This hardening effect due to rotation is particularly pronounced for the HP fabric where there is approximately an order of magnitude increase in the effective viscosity of ice to lateral shear.

6. Results

6.1. Characterization of the Ice-Surface Strain Field of Rutford Ice Stream

To place the ice fabric measurements in the context of ice deformation, we first characterize the ice-surface strain field of Rutford Ice Stream. The strain rates in the ice-flow coordinates, D_{tt}, D_{nn}, D_{tn}, are shown in Figures 6a–6c. In Figure 6d, the log-ratio, $\log_{10}\frac{|D_{tt}|}{|D_{tn}|}$, is used to quantify the magnitude of along-flow strain to lateral shear strain. Lateral shear dominates over horizontal uniaxial strain toward the ice-stream margin, whereas toward the center of the ice stream, along-flow uniaxial strain typically dominates over lateral shear. In the center of the ice stream, there is a spatial transition between compression and extension directions. Specifically, the "downstream central region" (sites A1–A3 and sites B1–B2) corresponds to weak along-flow compression/across-flow extension, whereas the "upstream central region" (sites B6–B10) corresponds to across-flow compression/along-flow extension.

The minimum horizontal strain rate (principal compression), $D_{\min}$, increases in magnitude toward the ice-stream margins (Figure 6e). The angle at which this principal compression acts is referenced to ice flow using $\theta_{\min} - \theta_t$ where $\theta_{\min}$ and θ_t are azimuthal bearing angles of the compression and ice-flow axes, respectively (Figure 6f). (An upstream convention is assumed so that $0 \le \theta_t < 180°$.) $\theta_{\min} - \theta_t = 0°$ corresponds to along-flow compression (approximately the case for the downstream region in the ice-stream center) and $\theta_{\min} - \theta_t = \pm 90°$ corresponds to across-flow compression (approximately the case for the upstream region). When the ice flow is dominated by lateral shear, it is a general result that $|\theta_{\min} - \theta_t| \to 45°$. This tendency can be understood from evaluating the principal (Mohr) angle formula

$$\theta_{\min} = \frac{1}{2}\arctan\left(\frac{2D_{tn}}{(D_{tt} - D_{nn})}\right), \tag{6}$$

when $2|D_{tn}| >> |D_{tt} - D_{nn}|$.

The uncertainty and fractional uncertainty on the minimum principal strain, $D_{\min}$, are shown in Figures 6g and 6h with the fractional uncertainty being appreciable (>0.5) in the central region of Transect A and downstream region of Transect B. The uncertainty on $\theta_{\min} - \theta_t$ is also highest (≈30°) in these regions (Figure 6i). The strain-rate magnitudes in Figure 6 are of order 10^{-3} a^{-1} and are of comparable magnitude to other Antarctic ice streams (K. E. Alley et al., 2018).

6.2. Ice Fabric Estimates

Polarimetric data analyses for three measurement sites along Transect A are shown in Figure 7 (refer Figures S2 and S3 in Supporting Information S1, for additional sites). A consistent feature is a band of high coherence magnitude, $|c_{hhvv}|$, in shallower ice, which extends to $z \approx 160$ m in the center of the ice stream (site A1) and $z \approx 80$ m toward the ice-stream margin (site A9). Therefore, to compare fabric estimates between sites we focus on $40 < z < 80$ m, which we refer to as unit U1, indicated in Figure 7c. Within U1, ϕ_{hhvv} and $d\phi_{hhvv}/dz$ are well-approximated by the backscatter simulation for depth-invariant principal axes (Figure 4a). A relative counterclockwise rotation of θ_y occurs between the center of the ice stream (Site A1: $\theta_y \approx 85°$ in U1) and closest to the ice-stream margin (Site A9: $\theta_y \approx 140°$ in U1). The azimuthal fabric strength generally increases toward the ice-stream margin, which is illustrated by the increasingly shallow depths of the first half-phase cycle ($\phi_{hhvv} = \pi$). At site A1 (Figure 7a), there is evidence for azimuthal fabric rotation within the ice column with θ_y in deeper ice rotated in a clockwise direction relative to shallower ice.

Polarimetric data analyses for three measurement sites along Transect B are shown in Figure 8 (refer Figures S4 and S5 in Supporting Information S1, for additional sites). The high-coherence band along Transect B generally extends to greater depth than along the majority of Transect A and extends to $z \approx 160$ m or greater at all measurement sites. For $z < 160$ m, sites B1–B6 are qualitatively similar to site A1 (directly downstream along the center streamline) and approximate the backscatter simulations for depth-invariant principal axes (Figure 4a).

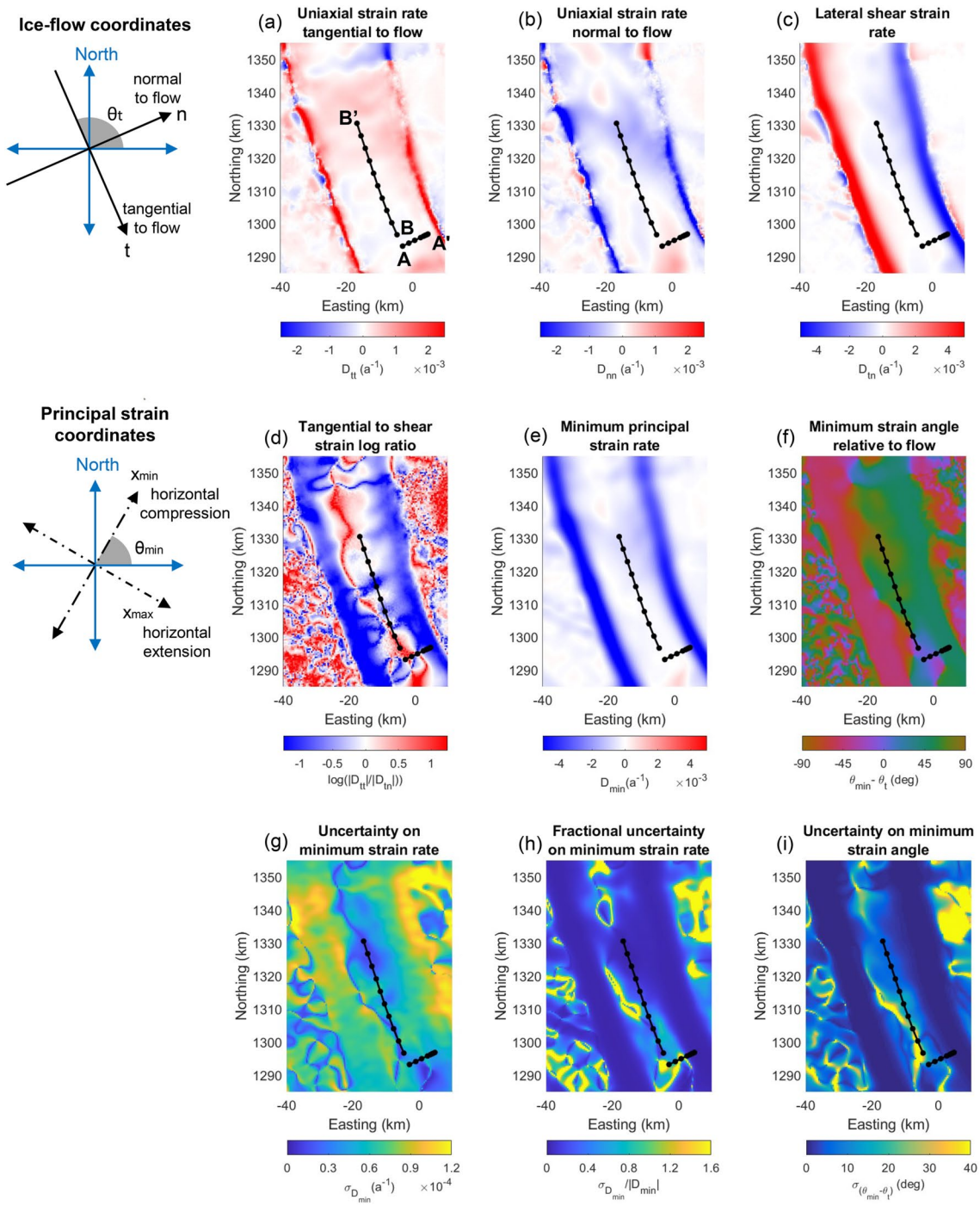

Figure 6. Characterization of the ice-surface strain field of Rutford Ice Stream. (a) Uniaxial strain rate tangential to ice flow (also called along-flow). (b) Uniaxial strain rate normal to ice flow (also called across-flow). (c) Lateral shear strain rate in ice-flow coordinates. (d) Flow-tangential to lateral shear strain log-ratio. (e) Minimum principal strain rate (horizontal compression). (f) Azimuthal angle of minimum strain (horizontal compression) relative to ice flow. (g) Uncertainty on minimum strain rate. (h) Fractional uncertainty on minimum strain rate. (i) Uncertainty on minimum strain angle relative to ice flow. Schematics for the ice-flow coordinates (t, n) and the principal strain coordinates (x_{min}, x_{max}) are shown. Panel (a) notates the measurement transects A and B.

By contrast, sites B8–B10 show two distinct subunits within the high coherence band (e.g., Figure 8c). These three sites all approximate the backscatter simulations for a 90° azimuthal rotation in ice fabric within the ice column (Figure 4b). The transition between the two units is at approximately 100 m depth. To compare fabric estimates between sites, we focus on two layers: $40 < z < 80$ m (U1, as defined for Transect A) and $120 < z < 160$ m

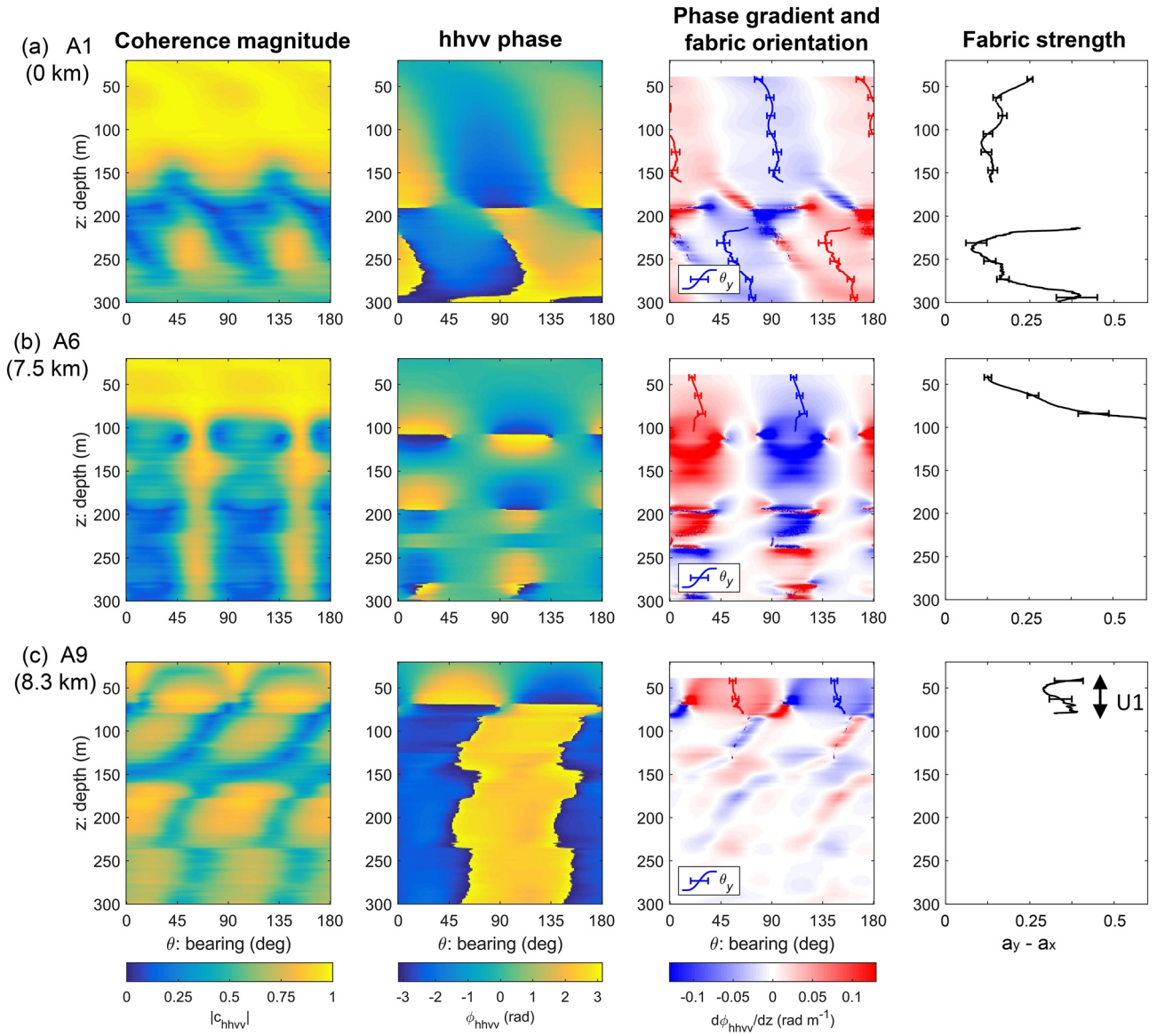

Figure 7. Polarimetric data analyses at three measurement sites along Transect A. (a) Site A1, (b) site A6, and (c) site A9. The depth profiles for the fabric estimates, $\theta_y(z)$ and $(a_y - a_x)(z)$ are shown in the center right and far right columns. A filtering step is applied such that fabric estimates require $|c_{hhvv}(\theta_y, z)| > 0.5$. The depth interval used to assess horizontal variation in ice fabric, U1, is shown in (c). The distance of each site along Transect A is indicated.

(U2). The gap between U1 and U2 is set to the coherence window size of 40 m so as not to bias the azimuthal fabric strength estimates. Within U1, there is evidence for a decrease in fabric strength toward the center of Transect B. Notably, Site B6 has a slower vertical phase cycle, which is further decreased at site B7 (see Supporting Information S1).

In general, the coherence magnitude is too low for the estimation of continuous ice fabric profiles for $z > 300$ m. The likely physical explanation for the transition from higher to lower coherence with ice depth is a depth transition from flatter to more buckled radar layers (E. King, 2009). The exception is a band of high coherence in deeper ice ($z > 1{,}400$ m), where the *hhvv* phase gradient is negligible (see Figure S6 in Supporting Information S1). We do not focus on this deeper-ice fabric in our data analysis as there is no azimuthal anisotropy present to constrain with radar sounding. However, due to general predictions of an increase in the vertical eigenvalue with ice depth, this deeper fabric is consistent with the presence of an azimuthally symmetric vertical cluster. Sites A10 and B1 were not included in the data analysis as fabric estimates could not be obtained within the unit depth intervals.

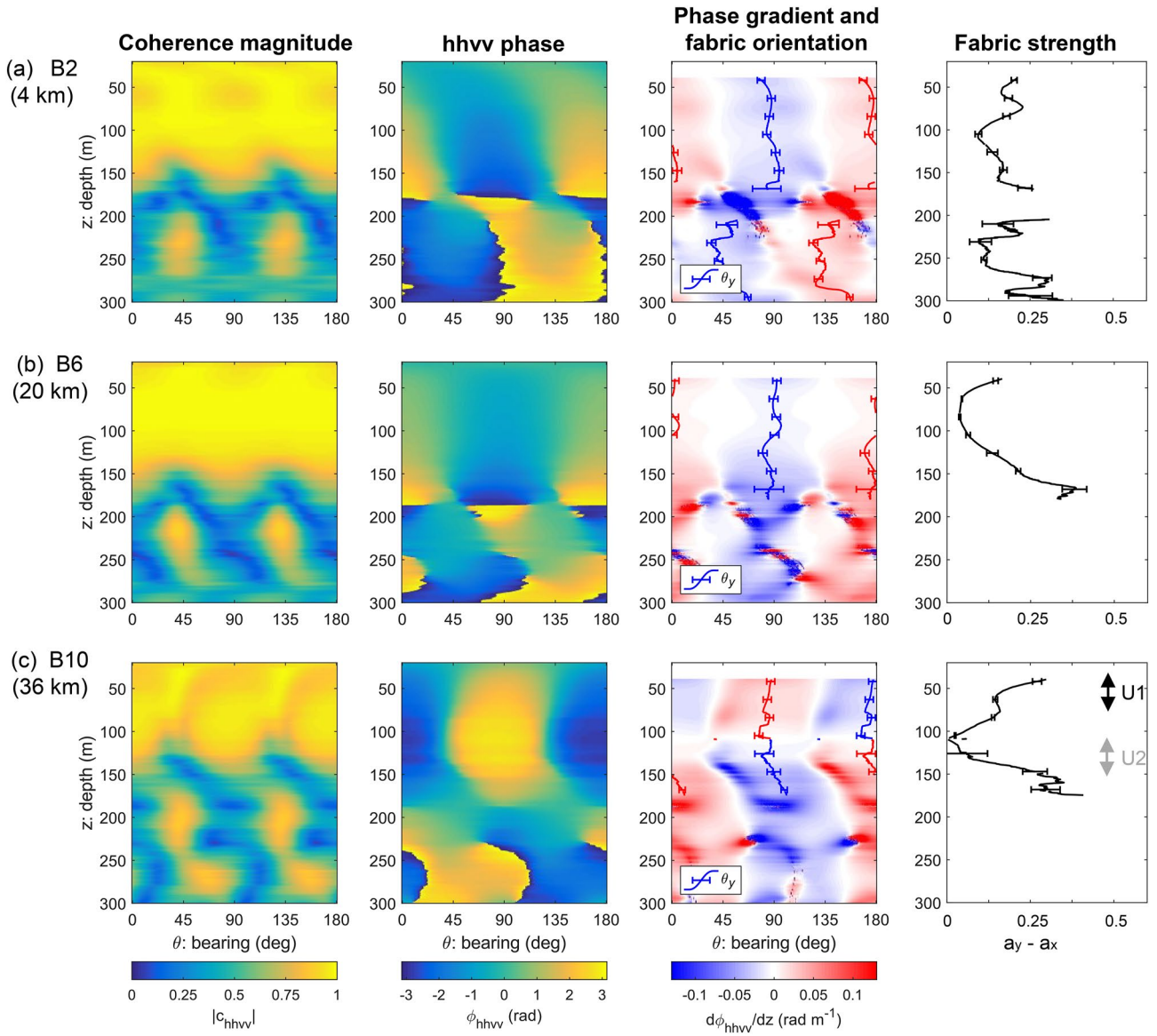

Figure 8. Polarimetric data analysis at three measurement sites along Transect B. (a) Site B2, (b) site B6, and (c) site B10. The depth profiles for the fabric estimates, $\theta_y(z)$ and $(a_y - a_x)(z)$, are shown in the center right and far right columns. A filtering step is applied such that fabric estimates require $|c_{hhvv}(\theta_y, z)| > 0.5$. The black and gray arrows in (c) indicate the two units U1 and U2. The distance of each site along Transect B is indicated.

6.3. Spatial Variation in Ice Crystal Orientation Fabric Within Rutford Ice Stream

The azimuthal orientation of the fabric, θ_y - θ_t, and principal compression, θ_{min} - θ_t, relative to ice flow are shown for unit U1 in Transect A (Figure 9a). The comparison is made to test the hypothesis that the fabric nearer the ice surface is consistent with strain-induced development that matches the local ice flow. The compression angle rotates counterclockwise from along-flow in the center of the ice stream (site A1) to 45° to flow toward the ice-stream margin (site A9). The fabric orientation is closely correlated with the compression angle, rotating counterclockwise by approximately 55° between sites A1 and A9. There is, however, a small systematic offset between the fabric and the compression angle (typically $\approx -10°$). The azimuthal fabric strength within U1 ranges from $a_y - a_x \approx 0.2$ at A1 to $a_y - a_x \approx 0.35$ at A9 and generally increases as the compressive strain rate, D_{min}, decreases (or equivalently $|D_{min}|$ increases) (Figure 9b).

Fabric estimates for units U1 and U2 in Transect B are shown in Figures 10a and 10b. In general, $\theta_y - \theta_t$ is better correlated with $\theta_{min} - \theta_t$ in U1 than U2. Notably, at the upstream sites B8–B10, the fabric and compression axes

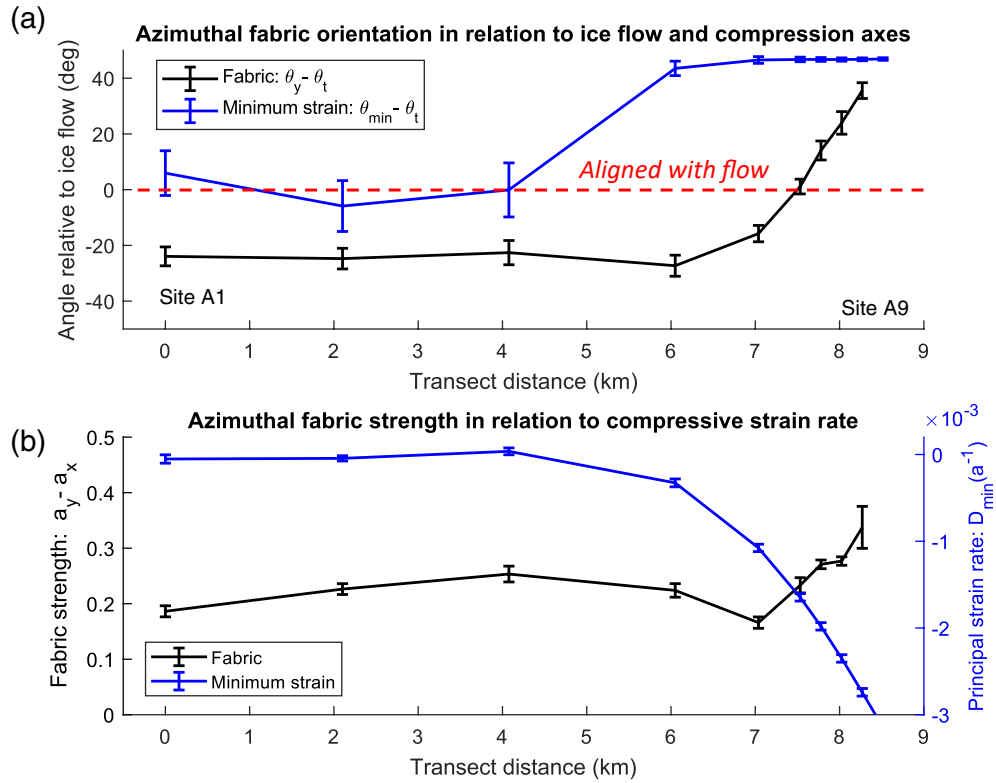

Figure 9. Spatial variation of ice fabric for unit U1 in Transect A in relation to ice-surface strain. (a) Azimuthal fabric orientation and horizontal compression axis relative to the ice-flow direction. (b) Azimuthal fabric strength and principal compression magnitude. The fabric estimates in U1 are depth-averaged over $40 < z < 80$ m.

are both orientated across-flow, whereas at the downstream site B2, the fabric and compression axes are both orientated along-flow. However, both $\theta_y - \theta_t$ and $a_y - a_x$ are less well correlated with D_{min} than along Transect A, particularly when $|D_{min}|$ is low at sites B3–B7. In unit U2, θ_y and $a_y - a_x$ are relatively constant along the entire length of Transect B with the fabric orientated along-flow and $a_y - a_x \approx 0.2$–0.25.

6.4. Spatial Variation in the Anisotropic Viscosity of Ice

The effective viscosity tensor elements (directional hardening of ice) in the ice-flow coordinates along Transect A (shallower ice: Unit 1) are shown in Figures 11a–11c. Similar to Figure 5, we show the three orientation models simultaneously, and the plot therefore represents the full range of viscosity that is consistent with the radar measurements.

In the central region of the ice stream (defined as sites A1–A3), uniaxial strain is either comparable to or greater in magnitude than shear strain (Figure 11d). Assuming the $\mathbf{x}_3$ vertical model applies as is likely (Lilien et al., 2021), the ice tends to be softer in the along-flow direction (where there is along-flow compression, $D_{tt} < 0$) than the across-flow direction (where there is across-flow extension, $D_{nn} > 0$). This result can be related to Figure 5b since the **t** axis is approximately aligned with the **y** axis, which is always the softer direction for the observed fabric strengths (for the case of $\mathbf{x}_2$ and $\mathbf{x}_3$ vertical models). It is to be noted, however, that η_{tttt} can be greater than η_{nnnn} for the lower a_z bound of the $\mathbf{x}_1$ vertical model (i.e., no crystals aligned in the horizontal plane) but this is thought to be an unlikely scenario in the central ice stream.

Along the entire length of Transect A, the softness of ice to lateral shear is dependent primarily on the choice of orientation model (Figure 11c) with the $\mathbf{x}_3$ vertical model resulting in ice being harder than isotropic ice to lateral shear and the $\mathbf{x}_1$ vertical model being softer than isotropic ice to lateral shear. In the marginal region (defined as sites A6–A9), lateral shear strain dominates over uniaxial strain (Figure 11d). In this marginal region, all three orientation models predict that ice locally hardens to lateral shear (i.e., η_{mtn} increases between sites A6 and A9),

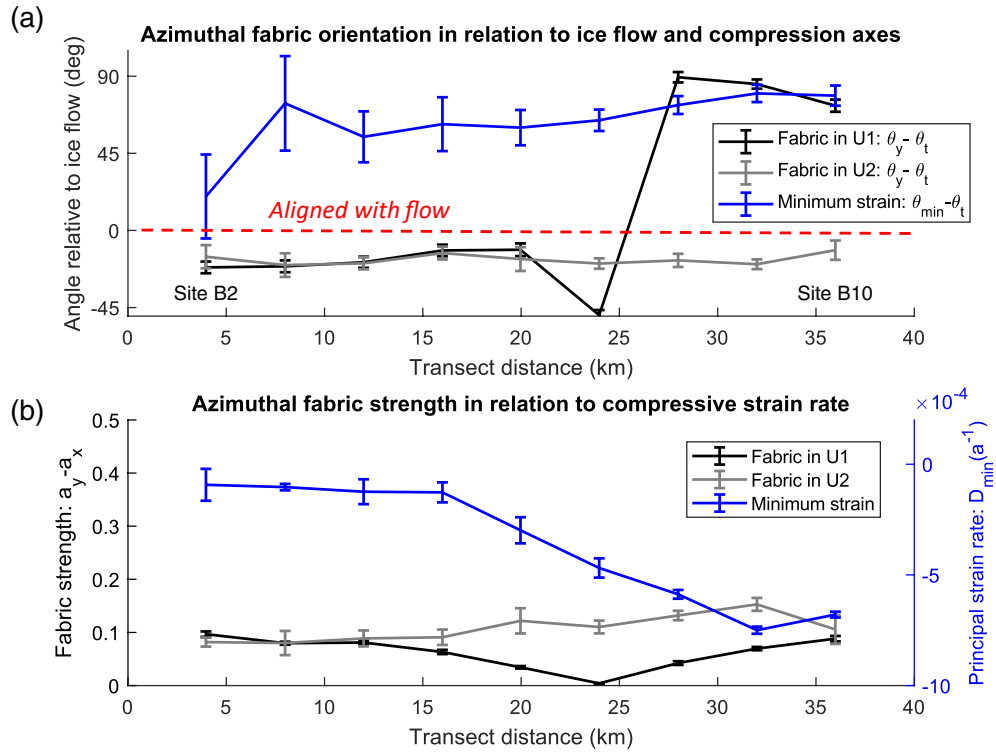

Figure 10. Spatial variation of ice fabric for unit U1 and U2 in Transect B in relation to ice-surface strain. (a) Azimuthal fabric orientation and horizontal compression axis relative to the ice-flow direction. (b) Azimuthal fabric strength and principal compression magnitude. The fabric estimates in U1 and U2 are depth-averaged over $40 < z < 80$ m and $120 < z < 160$ m, respectively.

so we highlight this as a key result that can be inferred from the radar. This local hardening relates to the rotation of the fabric away from the along-flow direction, and the result that η_{tntn} is generally harder than isotropic ice to shear at 45° degrees to ice flow (Figure 5e).

For Transect B, we describe the uniaxial viscosities for the two depth units (Figures 12a–12d) and the corresponding uniaxial surface strain rates (Figure 12e). As for the central region of Transect A, we assume that the $\mathbf{x}_3$ vertical model is most likely to apply. In shallower ice (Unit U1), there is an increase in η_{tttt} (relative hardening to along-flow uniaxial strain) moving upstream from site B2 to B10. On the other hand, there is a decrease in η_{nnnn} (relative softening to across-flow uniaxial strain) moving upstream. These results both relate to the rotation of the fabric relative to the ice-flow direction with the downstream region having the fabric (the softer **y** direction in Figure 5b) approximately aligned with ice flow and the upstream region having the fabric approximately perpendicular to ice flow. These results also correlate with the transition from weak along-flow compression ($D_{tt} < 0$) at site B2 to relatively strong across-flow compression at site B10 ($D_{nn} < 0$).

At sites B8-10, where the fabric has an order 90° rotation with ice depth (Figure 10), there is predicted to be a sharp transition in the anisotropic viscosities with depth. Specifically, η_{tttt} decreases between units U1 and U2 (ice softens to along-flow strain) and η_{nnnn} increases between units U1 and U2 (ice hardens to across-flow strain). These viscosity contrasts are most pronounced for the $\mathbf{x}_3$ vertical model, followed by the $\mathbf{x}_2$ vertical model. It is our expectation that the fabric can be represented between these two models in fast-flowing areas based on modeling results (Lilien et al., 2021) and seismic observations (Smith et al., 2017).

In the viscosity analysis, we also propagated the measurement uncertainties of fabric strength and orientation using an ensemble approach. This resulted in less than 5% fractional uncertainty for the viscosity bounds of each principal orientation model (the discrete points in Figures 11 and 12). We do not display this uncertainty graphically as it is small compared to possible viscosity range of the three models.

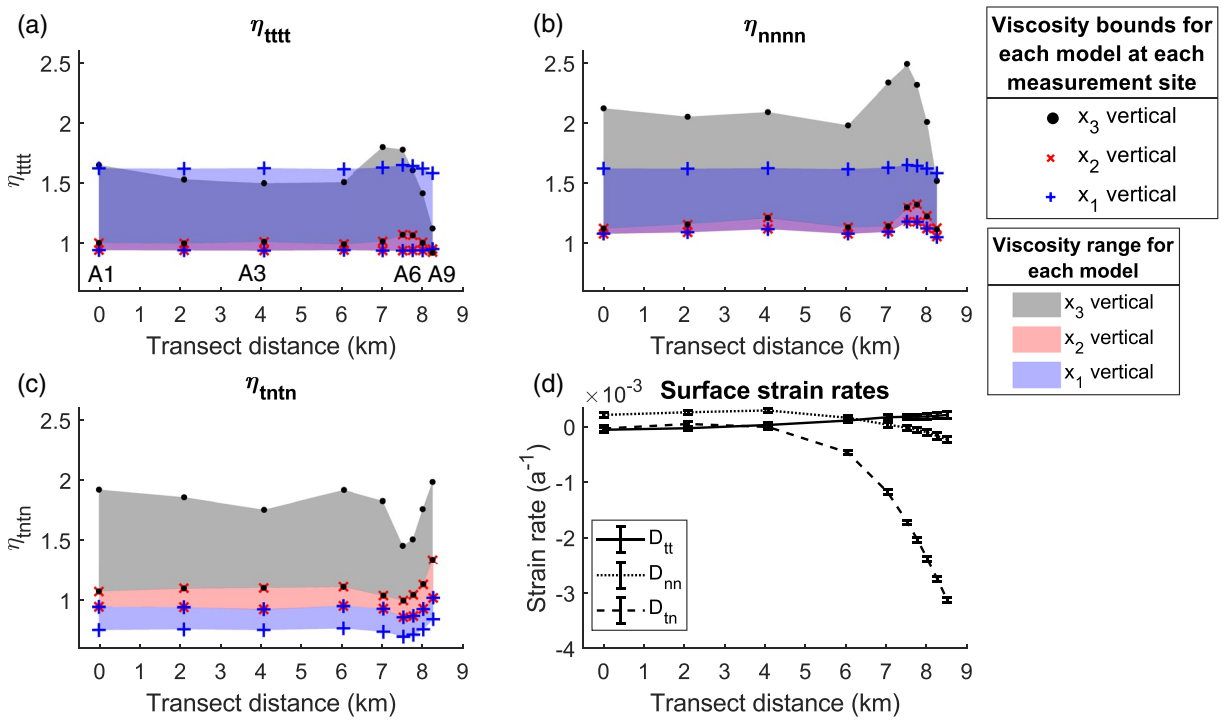

Figure 11. Effective viscosity tensor elements (directional hardening of ice) for Transect A. (a) Viscosity for uniaxial strain tangential to ice flow (also called along-flow) η_{tttt}. (b) Viscosity for uniaxial strain normal to ice flow η_{nnnn} (also called across-flow). (c) Viscosity for lateral shear η_{tntn}. (d) Surface strain rates in ice-flow coordinates. In (a)–(c), viscosities >1 indicate ice that is harder than isotropic ice.

7. Discussion

7.1. Flow-Induced Fabric Development in Ice Streams

An alignment between the principal compression direction and c-axis orientation is predicted for flow-induced fabric (also known as strain- or dynamically induced fabric) (Azuma & Higashi, 1985; R. B. Alley, 1988; van der Veen & Whillans, 1994). This relationship has been observed in various flow regimes across the ice sheets (e.g., Thorsteinsson et al., 1997; Wang et al., 2002), including in polarimetric radar-sounding studies (Brisbourne et al., 2019; Jordan, Schroeder, et al., 2020; K. Matsuoka et al., 2012). However, deviations from the simple relationship between compression and c-axis alignment are predicted for ice undergoing simple shear (Fujita & Mae, 1994; Llorens et al., 2016), which are supported by laboratory experiments (Qi et al., 2019). Specifically, for the case of an ideal horizontal pole, the c-axes are predicted to migrate toward being perpendicular to the shear plane due to an additional rigid body rotation, which results in fabric orientation deviating by 45° from the principal compression angle for the case of infinite strain (Fujita & Mae, 1994).

The fabric estimates in shallow ice within Rutford Ice Stream (unit U1) generally show a good correlation between crystal c-axis-preferred orientations and the compressive strain direction (Figures 9a and 10a). Notably, Transect A illustrates that the principal compression direction and fabric orientation both azimuthally rotate away from the flow direction (approaching 35° relative to ice flow near the ice-stream margin, Figure 9a). Transect A therefore illustrates that the predicted deviation from alignment with compression due to rigid body rotation (Azuma & Higashi, 1985; Fujita & Mae, 1994) is relatively small in the shallowest ice layer near the shear margin. An explanation for this discrepancy is that the shallow-ice fabric in U1 is in a transient state and still developing with ice depth. This interpretation is supported by the modeling in Llorens et al. (2016) where the c-axis orientation develops perpendicular to the direction of maximum finite shortening, which is initially 45° to the shear plane in simple shear and subsequently rotates toward perpendicular to the shear plane.

Inferred ice fabric orientation near to the eastern shear margin of Thwaites Glacier (Young, Schroeder, et al., 2021) is also consistent with the shear-margin fabric orientation results in this study. Specifically, birefringence loss

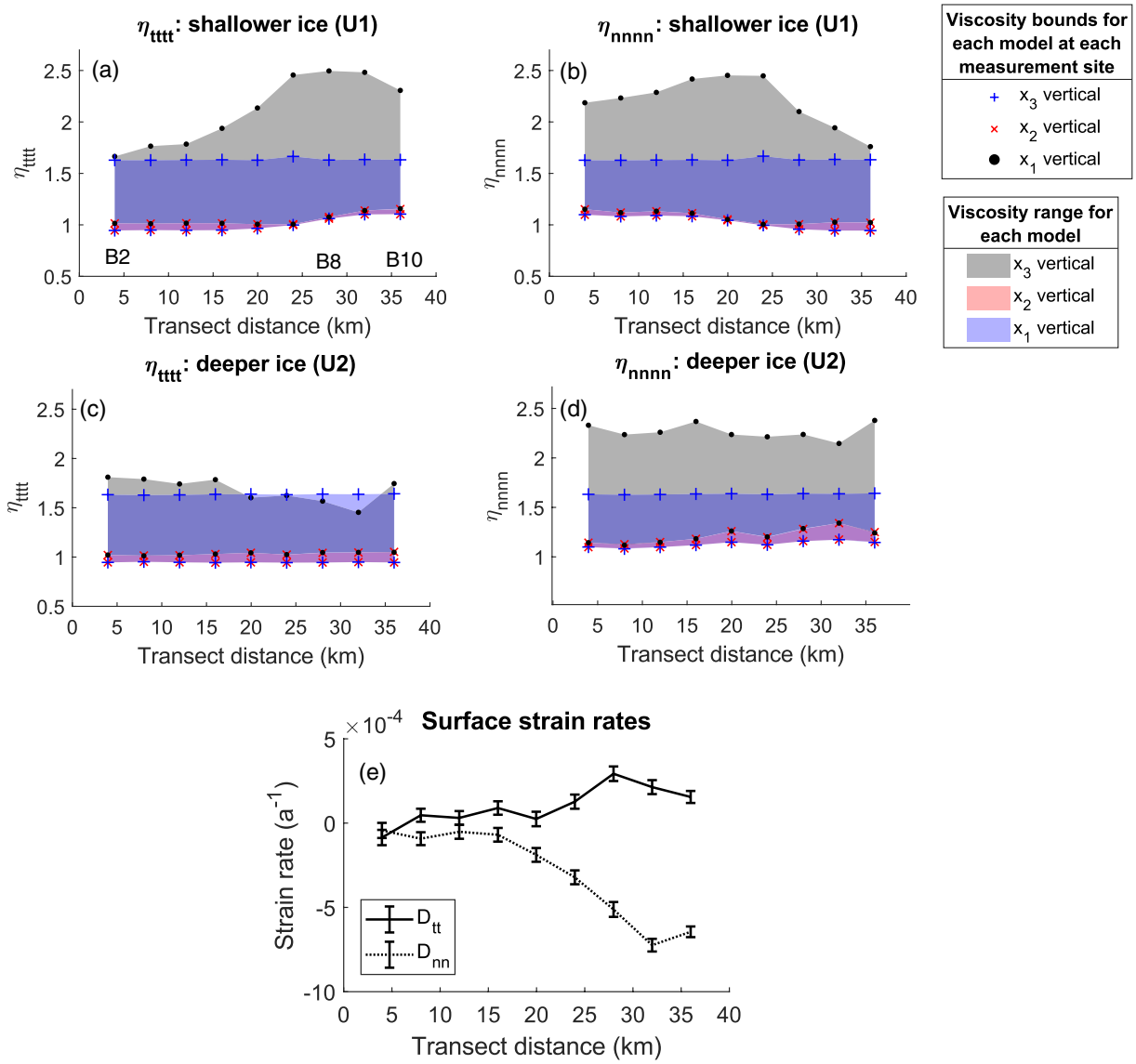

Figure 12. Effective viscosity tensor elements (directional hardening of ice) for Transect B. (a) Viscosity for uniaxial strain tangential to ice flow (along-flow) in shallower ice (unit U1). (b) Viscosity for uniaxial strain normal to ice flow (across-flow) in shallower ice (unit U1). (c) Viscosity for uniaxial strain tangential to ice flow (along-flow) in deeper ice (unit U2). (d) Viscosity for uniaxial strain normal to ice flow (across-flow) in deeper ice (unit U2). (e) Surface strain rates in ice-flow coordinates. In (a)–(d), viscosities >1 indicate ice that is harder than isotropic ice.

modulation of airborne radargrams indicates that the fabric near the margin is significantly weaker than a horizontal pole fabric and not orientated perpendicular or parallel to flow.

The correlation between the orientation of the shallow-ice fabric and the compression angle generally increases with the compressive strain rate as does the azimuthal strength of the fabric (Figures 9 and 10). These observations suggest that larger strain rates result in a faster rate of fabric development. However, the relatively coarse resolution of the strain field (limited by the filter width in the spatial derivative) impedes a refined estimation of the length- and time scales for fabric development.

An important caveat when interpreting our results is that, due to bed topography, the downstream region of the central ice stream (sites A1-A3 and B2) is an atypical deformation regime for an ice stream. Specifically, this region corresponds to relatively weak along-flow compression and across-flow extension (Figure 6). By contrast, the upstream region of Transect B is likely to be more representative with along-flow extension and across-flow compression present.

7.2. Azimuthal Fabric Rotation Within the Ice Column

A particularly striking result is the azimuthal rotation of nearly 90° within the ice column between units U1 and U2 at the upstream region of Transect B (Figure 8c.) A consequence of this rotation is that the fabric orientation in deeper ice (unit U2, fabric orientation along-flow) is significantly misaligned with the across-flow surface compression axis (Figure 10). Analogous behavior (i.e., better alignment between surface compression and fabric in shallower ice than deeper ice) has been noted in other polarimetric radar-sounding studies at ice divides (K. Matsuoka et al., 2012), ice rises (Brisbourne et al., 2019), and within Whillans Ice Stream (Jordan, Schroeder, et al., 2020).

For consistency with flow-induced fabric development, the fabric orientation in unit U2 implies that the ice is undergoing (or has undergone) along-flow compression. This assertion is supported by the presence of along-flow compression in the surface ice ≈20–30 km upstream of site B10 (Figure 6). Specifically, this observation is consistent with the fabric in U2 developing upstream in the near surface, then being advected horizontally and buried vertically to its current location. Alternatively, temporal changes in the surface strain field could contribute to the observed difference between the surface strain and unit U2. On a related note, the systematic offset between the fabric orientation and the compression axis for Transect A (Figure 9) is likely to be explained by advection although temporal changes in the surface strain field cannot be excluded.

7.3. The Impact of Ice Fabric on Anisotropic Viscosity

The clear limitation in deriving anisotropic viscosity from radar-sounding fabric measurements is that the vertical component of the orientation tensor is unknown. In turn, this results in a range of anisotropic viscosities that are consistent with each radar fabric measurement (shown for the general case in Figure 5, and for the measurements in Rutford Ice Stream in Figures 11 and 12). Despite these limitations, we propose that the radar measurements can be used to interpret local changes in effective viscosity, particularly, as variation in the vertical fabric component should be small relative to the horizontal component when assessing lateral variation along the radar transects.

A seemingly counterintuitive result is that the rotation of the near-surface fabric toward the compression axis near the shear margin (sites A6–A9) results in local hardening of the ice to lateral shear (Figure 11c). This finding differs from Minchew et al. (2018) who, via a model-based approach, inferred that the fabric has a softening effect on lateral shear in the margins of Rutford Ice Stream, consistent with the shear-margin fabric being a horizontal pole where the c-axes are aligned with ice flow (Figure 5c). (It is to be noted that the softening of ice to shear is normally discussed for the analogous scenario of ice being soft to horizontal shearing within the ice column due to a vertical pole; Azuma & Goto-Azuma, 1996; Ma et al., 2010). Therefore, to reconcile our results with Minchew et al. (2018), we propose that fabric and viscosity of the shallow-ice layer near the shear margin are likely to be unrepresentative of the majority of the ice column, and the fabric that enhances lateral shear could conceivably be present in deeper ice.

A general result is that ice has lower effective viscosity to uniaxial strain in the direction of horizontal c-axis alignment than in the orthogonal horizontal direction (represented by the fact that $\eta_{yyyy} \leq \eta_{xxxx}$ in Figure 5). This result can be used to interpret both lateral and depth variations in the uniaxial viscosities. Regarding lateral variation of viscosity, a key result is the spatial transition from ice being softer to across-flow strain in the upstream region (sites B8–B10) to ice being softer to along-flow strain in the downstream region (site B2).

An important consequence of azimuthal fabric rotation within the ice column is that it results in a depth-transition in the anisotropic effective viscosity of ice. Specifically, upstream at sites B8-B10, shallower ice (U1) is harder for along-flow strain than across flow whereas deeper ice (U2) is harder for across-flow strain than along-flow (Figure 12). This result has particular significance for studies that use ice-surface strain information within inverse ice-sheet modeling (Goldberg, 2011; Hindmarsh, 2004; MacAyeal, 1992; Schoof & Hindmarsh, 2010). In particular, fabric changes with ice depth are associated with anisotropic viscosity changes with ice depth, and isotropic models generally do not account for that when deriving basal conditions.

7.4. Comparison With Previous Seismic Measurements of Fabric Within Rutford Ice Stream

Previous studies of ice column fabric within Rutford Ice Stream, utilizing seismic shear-wave splitting observations (Harland et al., 2013; Smith et al., 2017), observe both vertical and azimuthal anisotropy. Both studies used icequakes from the bed of the ice stream ($z > 2{,}000$ m) recorded at surface stations over a 7-km-wide section of the central ice stream in the vicinity of sites A1 and B2. The more comprehensive study of Smith et al. (2017) synthesized splitting observations with an average ice-column fabric combining an azimuthally symmetric vertical cluster and an azimuthally anisotropic "horizontal partial girdle" (HPG), similar in form to the fabrics presented here. The vertical cluster component, which relates to the strength of the vertical fabric eigenvalue, cannot be directly characterized with radar sounding. However, the deeper-ice data (see Figure S6 in Supporting Information S1) support that the cluster dominates at ice depth $z > 1{,}400$ m as there is no evidence for significant azimuthal anisotropy over this depth range.

The shear-wave splitting method samples a column-averaged fabric between the ice stream bed and the surface. Under certain conditions, the method can be used to discriminate layered fabric structures. However, Smith et al. (2017) were unable to detect discrete layering in their observations and assumed a homogeneous anisotropic diffuse medium throughout the ice column. Both radar and seismic data sets indicate azimuthal anisotropy although there are differing orientations for the direction of greatest horizontal c-axis alignment. Specifically, in unit U2 of this study (the deepest ice considered from 120–160 m), the fabric (greatest horizontal c-axis alignment) is aligned approximately parallel to flow. However, in the seismic interpretation of the full ice column by Smith et al. (2017), the fabric of the bulk ice column is perpendicular to flow. Although we are unable to directly explain these discrepancies, it is likely that a combination of the inherent spatial- and depth-averaging nature of the seismic method and a lower sensitivity to thin layers results in the smaller-scale structure presented here being subsumed into a bulk fabric interpretation. We can, however, conclude that it is unlikely that unit U2 is representative of the rest of the ice column, and a fabric more similar to that presented by Smith et al. (2017) is likely to dominate in deeper ice.

8. Summary and Conclusions

In this study, we used polarimetric radar sounding to investigate controls on the spatial development of ice crystal orientation fabric within the near surface (top 40–300 m) of Rutford Ice Stream. We then used the radar fabric estimates to parameterize an anisotropic flow law and assess the impact of the fabric on the anisotropic viscosity (directional hardening) of ice. Our study revealed pronounced lateral and depth variations in both fabric and anisotropic viscosity within the flow unit with clear relationships to the ice-surface strain field present.

The main conclusions are:

1. *Fabric in the shallowest ice within ice streams is generally well aligned with surface compression.* The radar characterization of azimuthal fabric anisotropy in the shallowest ice (top 40–100 m) is consistent with fabric resulting from finite strain and flow-induced development. This finding confirms expected behavior (i.e., correlation between the horizontal compression axis and direction of greatest horizontal *c*-axis alignment) and highlights that the fabric responds to locally variable (<5 km scale) changes in the horizontal compression direction. Of particular note, at the ice-stream margins, there is a tendency for the horizontal compression axis and the fabric to be oriented toward 45° to the ice-flow direction, which is consistent with the early stages of fabric development under simple shear.
2. *Deeper ice-stream fabric can be significantly misaligned from the surface compression due to azimuthal rotation of fabric.* The radar measurements in the center of the ice stream show that in deeper ice (greater than 100 m), the fabric can be azimuthally rotated from the surface compression direction (including a misalignment of ≈90° in extreme cases). Due to misalignment with the local strain field and better alignment with the upstream strain field, our results suggest that ice-stream fabric is induced near the surface and preserved during downstream transport.
3. *Spatial variation in ice fabric translates to lateral and depth variations in the anisotropic viscosity of ice.* We showed that despite being limited to measuring horizontal fabric properties, radar-sounding can be used to constrain local changes in anisotropic viscosity. Toward the shear margin (where we could only interpret the top 100 m of ice), we did not find evidence for fabric softening ice to lateral shear. In the center of the ice stream, we showed that depth-transitions in ice fabric are associated with depth changes in anisotropic

viscosity. The lack of correlation between the surface strain rates and the deeper englacial fabric represents a new challenge for models that invert for basal conditions and viscosity from surface strain-rates assuming simplified vertical variation of ice viscosity.

Data Availability Statement

Polarimetric radar sounding data are available via NERC's Polar Data Centre: https://doi.org/10.5285/D5B7E5A1-B04D-48D8-A440-C010658EC146 (Brisbourne et al., 2020). The MEaSURES ice velocity data products are available at NSIDC: https://doi.org/10.5067/D7GK8F5J8M8R (Rignot et al., 2017). The AI GOLF flow solver is available as part of the Elmer ice git repository at: https://github.com/ElmerCSC/elmerfem/blob/devel/elmerice/Solvers/GolfLaw.F90 (Gillet-Chaulet et al., 2014).

Acknowledgments
Radar data were collected as part of the BEAMISH Project (NERC AFI award numbers NE/G014159/1 and NE/G013187/1). We are grateful to Rebecca Schlegel and Anne Flink for assistance with data acquisition. We would like to thank two anonymous reviewers for their insightful and constructive reviews and TJ Young, University of Cambridge, for his helpful comments. TMJ would like to acknowledge support from EU Horizons 020 Grant 747336-BRISR ES-H2020-MSCA-IF-2016. DMS was supported, in part, by NSF CAREER Award 1745137.

References

Alley, K. E., Scambos, T. A., Anderson, R. S., Rajaram, H., Pope, A., & Haran, T. M. (2018). Continent-wide estimates of Antarctic strain rates from Landsat 8-derived velocity grids. *Journal of Glaciology*, *64*(244), 321–332. https://doi.org/10.1017/jog.2018.23

Alley, R. B. (1988). Fabrics in polar ice sheets: Development and prediction. *Science*, *240*(4851), 493–495. https://doi.org/10.1126/science.240.4851.493

Azuma, N., & Goto-Azuma, K. (1996). An anisotropic flow-law for ice-sheet ice and its implications. *Annals of Glaciology*, *23*, 201–208. https://doi.org/10.1016/0012-821X(94)90173-2

Azuma, N., & Higashi, A. (1985). Formation processes of ice fabric pattern in ice sheets. *Annals of Glaciology*, *6*, 130–134. https://doi.org/10.3189/1985AoG6-1-130-134

Boerner, W. M. (1992). Basic concepts in radar polarimetry: Polsarpro v3.0. ESA Earth Online. https://doi.org/10.1029/96JB00412

Brennan, P. V., Lok, L. B., Nicholls, K., & Corr, H. (2014). Phase-sensitive FMCW radar system for high-precision Antarctic ice shelf profile monitoring. *IET Radar, Sonar & Navigation*, *8*(7), 776–786. https://doi.org/10.1049/iet-rsn.2013.0053

Brisbourne, A. M., Jordan, T. M., Martin, C., Schroeder, D. M., & Smith, A. M. (2020). Radar characterization of ice crystal orientation fabric and anisotropic rheology within rutford ice stream, 2017-2019 [dataset]. NERC Polar Data Centre. https://doi.org/10.5285/D5B7E5A1-B04D-48D8-A440-C010658EC146

Brisbourne, A. M., Martin, C., Smith, A. M., Baird, A. F., Kendall, J. M., & Kingslake, J. (2019). Constraining recent ice flow history at Korff ice rise, West Antarctica, using radar and seismic measurements of ice fabric. *Journal of Geophysical Research: Earth Surface*, *124*(175), 194–373. https://doi.org/10.1029/2018JF004776

Budd, W. F., Warner, R. C., Jacka, T. H., Li, J., & Treverrow, A. (2013). Ice flow relations for stress and strain-rate components from combined shear and compression laboratory experiments. *Journal of Glaciology*, *59*(214), 374–392. https://doi.org/10.3189/2013JoG12J106

Castelnau, O., Duval, P., Lebensohn, R. A., & Canova, G. R. (1996). Viscoplastic modeling of texture development in polycrystalline ice with a self-consistent approach: Comparison with bound. *Journal of Geophysical Research*, *101*(B6), 13851–13868. https://doi.org/10.1029/96JB00412

Cuffey, K., & Paterson, W. S. B. (2010). *The physics of glaciers* (n). Academic Press. chapter 3.

Dall, J. (2009). Polarimetric ice sounding at p-band: First results. *IEEE 2009 international geoscience and Remote sensing symposium (IGARSS 2009)*, 1024–1027.

Dall, J. (2010). Ice sheet anisotropy measured with polarimetric ice sounding radar. *30th international geoscience and Remote sensing symposium (IGARSS 2010), 25–30 july 2010*, 2507–2510.

Doake, C. S. M., Corr, H. F. J., Jenkins, A., Nicholls, K. W., & Stewart, C. (2003). Interpretation of polarization behaviour of radar waves transmitted through Antarctic ice shelves. *Proceedings of the Workshop on POLinSAR—Applications of SAR Polarimetry and Polarimetric Interferometry*, 1–8. (ESA SP-529).

Ershadi, M. R., Drews, R., Martín, C., Eisen, O., Ritz, C., Corr, H., et al. (2021). Polarimetric radar reveals the spatial distribution of ice fabric at domes in East Antarctica. *The Cryosphere Discussions*, *2021*, 1–34. https://doi.org/10.5194/tc-2020-370

Faria, S. H., Weikusat, I., & Azuma, N. (2014). The microstructure of polar ice. Part II: State of the art. *Journal of Structural Geology*, *61*, 21–49. https://doi.org/10.1016/j.jsg.2013.11.003

Fujita, S., & Mae, S. (1994). Strain in the ice sheet deduced from the crystal-orientation fabrics fro, bare icefields adjacent to the Sor-Rondane Mountains, Dronning Maud Land, East Antarctica. *Journal of Glaciology*, *40*(134), 135–139. https://doi.org/10.3189/S0022143000003907

Fujita, S., Maeno, H., & Matsuoka, K. (2006). Radio-wave depolarization and scattering within ice sheets: A matrix-based model to link radar and ice-core measurements and its application. *Journal of Glaciology*, *52*(178), 407–424. https://doi.org/10.3189/172756506781828548

Fujita, S., Maeno, H., Uratsuka, S., Furukawa, T., Mae, S., Fujii, Y., & Watanabe, O. (1999). Nature of radio echo layering in the Antarctic ice sheet detected by a two-frequency experiment. *Journal of Geophysical Research*, *104*(10), 13. https://doi.org/10.1029/1999JB900034

Fujita, S., Matsuoka, T., Ishida, T., Matsuoka, K., & Mae, S. (2000). A summary of the complex dielectric permittivity of ice in the megahertz range and its applications for radar sounding of polar ice sheets. *Physics of Ice Core Records*, *104*, 185–212.

Gagliardini, O., Gillet-Chaulet, F., & Montagnat, M. (2009). A review of anisotropic polar ice models: From crystal to ice-sheet flow models. *Low Temperature Science*, *68*, 149–166.

Gagliardini, O., & Meyssonnier, J. (1999). Analytical derivations for the behavior and fabric evolution of a linear orthotropic ice polycrystal. *Journal of Geophysical Research*, *104*(B8), 17797–17809. https://doi.org/10.1029/1999JB900146

Gagliardini, O., Zwinger, T., Gillet-Chaulet, F., Durand, G., Favier, L., deFleurian, B., et al. (2013). Capabilities and performance of elmer/ice, a new-generation ice sheet model. *Geoscientific Model Development*, *6*(4), 1299–1318. https://doi.org/10.5194/gmd-6-1299-2013

Gillet-Chaulet, F., Gagliardini, M. J., Zwinger, T., & Ruokolainen, J. (2006). Flow-induced anisotropy in polar ice and related ice-sheet flow modelling. *Journal of Non-Newtonian Fluid Mechanics*, *134*(1–3), 33–43. https://doi.org/10.1016/j.jnnfm.2005.11.005

Gillet-Chaulet, F., Gagliardini, O., & Durand, G. (2014). Golf law in elmer ice [software]. Retrieved from https://github.com/ElmerCSC/elmerfem/blob/devel/elmerice/Solvers/GolfLaw.F90

Gillet-Chaulet, F., Gagliardini, O., Meyssonnie, J., Montagnat, M., & Castelnau, O. (2005). A user-friendly anisotropic flow law for ice-sheet modelling. *Journal of Glaciology*, *51*(172), 3–14. https://doi.org/10.3189/172756505781829

Glen, J. W. (1954). The creep of polycrystalline ice. *Proceedings of the Royal Society of London A*, *228*(1175), 519–538. https://doi.org/10.1098/rspa.1955.0066

Godert, G. (2003). A mesoscopic approach for modelling texture evolution of polar ice including recrystallization phenomena. *Annals of Glaciology*, *37*, 1–28. https://doi.org/10.3189/172756403781815375

Goldberg, D. N. (2011). A variationally derived, depth-integrated approximation to a higher-order glaciological flow model. *Journal of Glaciology*, *57*(201), 157–170. https://doi.org/10.3189/002214311795306763

Graham, F. S., Morlighem, M., Warner, R. C., & Treverrow, A. (2018). Implementing an empirical scalar constitutive relation for ice with flow-induced polycrystalline anisotropy in large-scale ice sheet models. *The Cryosphere*, *12*(3), 1047–1067. https://doi.org/10.5194/tc-12-1047-2018

Greene, C. A., Gwyther, D. E., & Blankenship, D. D. (2017). Antarctic Mapping Tools for Matlab. *Computational Geosciences*, *104*(C), 151–157. https://doi.org/10.1016/j.cageo.2016.08.003

Hargreaves, N. D. (1978). The radio-frequency birefringence of polar ice. *Journal of Glaciology*, *21*(85), 301–313. https://doi.org/10.3189/s0022143000033499

Harland, S., Kendall, J.-M., Stuart, G., Lloyd, G., Baird, A., Smith, A., et al. (2013). Deformation in rutford ice stream, West Antarctica: Measuring shear-wave anisotropy from icequakes. *Annals of Glaciology*, *54*(64), 105–114. https://doi.org/10.3189/2013AoG64A033

Hindmarsh, R. C. A. (2004). A numerical comparison of approximations to the Stokes equations used in ice sheet and glacier modeling. *Journal of Geophysical Research*, *109*(F1). https://doi.org/10.1029/2003JF000065

Horgan, H. J., Anandakrishnan, S., Alley, R. B., Burkett, P. G., & Peters, L. E. (2011). Englacial seismic reflectivity: Imaging crystal-orientation fabric in West Antarctica. *Journal of Glaciology*, *57*(204), 639–650. https://doi.org/10.3189/002214311797409686

Jackson, M., & Kamb, B. (1997). The marginal shear stress of Ice Stream B, West Antarctica. *Journal of Glaciology*, *43*(145), 415–426. https://doi.org/10.3189/S0022143000035000

Jordan, T. M., Besson, D. Z., Kravchenko, I., Latif, U., Madison, B., Nokikov, A., & Shultz, A. (2020). Modeling ice birefringence and oblique radio wave propagation for neutrino detection at the South Pole. *Annals of Glaciology*, *61*(81), 84–91. https://doi.org/10.1017/aog.2020.18

Jordan, T. M., Schroeder, D. M., Castelletti, D., Li, J., & Dall, J. (2019). A polarimetric coherence method to determine ice crystal orientation fabric from radar sounding: Application to the NEEM ice core region. *IEEE Transactions on Geoscience and Remote Sensing*, *57*(11), 1–17. https://doi.org/10.1109/TGRS.2019.2921980

Jordan, T. M., Schroeder, D. M., Elsworth, C. W., & Siegfried, M. R. (2020). Estimation of ice fabric within Whillans Ice Stream using polarimetric phase-sensitive radar sounding. *Annals of Glaciology*, *61*(81), 74–83. https://doi.org/10.1017/aog.2020.6

King, E. (2009). Flow dynamics of the Rutford Ice Stream ice-drainage basin, West Antarctica, from radar stratigraphy. *Annals of Glaciology*, *50*(51), 42–48. https://doi.org/10.3189/172756409789097586

King, E. C., Pritchard, H. D., & Smith, A. M. (2016). Subglacial landforms beneath Rutford ice stream, Antarctica: Detailed bed topography from ice-penetrating radar. *Earth System Science Data*, *8*(1), 151–158. https://doi.org/10.5194/essd-8-151-2016

Kluskiewicz, D., Waddington, E. D., Anandakrishnan, S., Voigt, D. E., Matsuoka, K., & McCarthy, M. P. (2017). Sonic methods for measuring crystal orientation fabric in ice, and results from the West Antarctic Ice Sheet (WAIS) Divide. *Journal of Glaciology*, *63*(240), 603–617. https://doi.org/10.1017/jog.2017.20

Li, J., González, J. A. V., Leuschen, C., Harish, A., Gogineni, P., Montagnat, M., et al. (2018). Multi-channel and multi-polarization radar measurements around the NEEM site. *The Cryosphere*, *12*(8), 2689–2705. https://doi.org/10.5194/tc-12-2689-2018

Lilien, D. A., Rathmann, N. M., Hvidberg, C. S., & Dahl-Jensen, D. (2021). Modeling ice-crystal fabric as a proxy for ice-stream stability. *Journal of Geophysical Research: Earth Surface*, *126*(9), e2021JF006306. https://doi.org/10.1029/2021JF006306

Llorens, M.-G., Griera, A., Bons, P. D., Lebensohn, R. A., Evans, L. A., Jansen, D., & Weikusat, I. (2016). Full-field predictions of ice dynamic recrystallisation under simple shear conditions. *Earth and Planetary Science Letters*, *450*, 233–242. https://doi.org/10.1016/j.epsl.2016.06.045

Ma, Y., Gagliardini, O., Ritz, C., Gillet-Chaulet, F., & Montagnat, M. (2010). Enhancement factors for grounded ice and ice shelves inferred from an anisotropic ice-flow model. *Journal of Glaciology*, *56*(199), 805–812. https://doi.org/10.3189/002214310794457209

MacAyeal, D. R. (1992). The basal stress-distribution of Ice Stream-E, Antarctica, inferred by control methods. *Journal of Geophysical Research*, *97*(B1), 595–603. https://doi.org/10.1029/91JB02454

Martin, C., Gudmundsson, G. H., Pritchard, H. D., & Gagliardini, O. (2009). On the effects of anisotropic rheology on ice flow, internal structure, and the age-depth relationship at ice divides. *Journal of Geophysical Research*, *114*(4), 1–18. https://doi.org/10.1029/2008JF001204

Matsuoka, K., Power, D., Fujita, S., & Raymond, C. F. (2012). Rapid development of anisotropic ice-crystal-alignment fabrics inferred from englacial radar polarimetry, central West Antarctica. *Journal of Geophysical Research*, *117*(3), 1–16. https://doi.org/10.1029/2012JF002440

Matsuoka, K., Wilen, L., Hurley, S., & Raymond, C. (2009). Effects of Birefringence Within Ice Sheets on Obliquely Propagating Radio Waves. *IEEE Transactions on Geoscience and Remote Sensing*, *47*(5), 1429–1443. https://doi.org/10.1109/TGRS.2008.2005201

Matsuoka, T., Fujita, S., & Mae, S. (1996). Effect of temperature on dielectric properties of ice in the range 5 − 39 GHz. *Journal of Applied Physics*, *80*(109), 5884–5890. https://doi.org/10.1063/1.363582

Minchew, B. M., Meyer, C. R., Robel, A. A., Gudmundsson, G. H., & Simons, M. (2018). Processes controlling the downstream evolution of ice rheology in glacier shear margins: Case study on rutford ice stream, West Antarctica. *Journal of Glaciology*, *64*(248), 583–594. https://doi.org/10.1017/jog.2018.47

Minchew, B. M., Simons, B., Riel, B., & Milillo, P. (2016). Tidally induced variations in vertical and horizontal motion on Rutford Ice Stream, West Antarctica, inferred from remotely sensed observations. *Journal of Geophysical Research: Earth Surface*, *122*(1), 167–190. https://doi.org/10.1002/2016JF003971

Montagnat, M., Azuma, N., Eichler, J., Fujita, S., Kipfstuhl, S., Gillet-Chaulet, F., et al. (2014). Fabric along the NEEM ice core, Greenland, and its comparison with GRIP and NGRIP ice cores. *The Cryosphere*, *8*(4), 1129–1138. https://doi.org/10.5194/tc-8-1129-2014

Ng, F. (2015). Spatial complexity of ice flow across the Antarctic Ice Sheet. *Nature Geoscience*, *8*(11), 847—850–850. https://doi.org/10.1038/ngeo2532

Nicholls, K. W., Corr, H. F. J., Stewart, C. L., Lok, L. B., Brennan, P. V., & Vaughan, D. G. (2015). A ground-based radar for measuring vertical strain rates and time-varying basal melt rates in ice sheets and shelves. *Journal of Glaciology*, *61*(230), 1079–1087. https://doi.org/10.3189/2015JoG15J073

Pettit, E. C., Thorsteinsson, T., Jacobson, H. P., & Waddington, E. D. (2007). The role of crystal fabric in flow near an ice divide. *Journal of Glaciology*, *53*(181), 277–288. https://doi.org/10.3189/172756507782202766

Picotti, S., Vuan, A., Carcione, J. M., Horgan, H. J., & Anandakrishnan, S. (2015). Anisotropy and crystalline fabric of Whillans Ice Stream (West Antarctica) inferred from multicomponent seismic data. *Journal of Geophysical Research: Solid Earth*, *120*(6), 4237–4262. https://doi.org/10.1002/2014JB011591

Qi, C., Prior, D. J., Craw, L., Fan, S., Llorens, M.-G., Griera, A., et al. (2019). Crystallographic preferred orientations of ice deformed in direct-shear experiments at low temperatures. *The Cryosphere*, *13*(1), 351–371. https://doi.org/10.5194/tc-13-351-2019

Rathmann, N. M., Lilien, D. A., Grinsted, A., Gerber, T. A., Young, T. J., & Dahl-Jensen, D. (2022). On the limitations of using polarimetric radar sounding to infer the crystal orientation fabric of ice masses. *Geophysical Research Letters*, *49*(1), e2021GL096244. https://doi.org/10.1029/2021gl096244

Rignot, E., Mouginot, J., & Scheuchl, B. (2011). Ice flow of the Antarctic ice sheet. *Science*, *33*(6048), 1427–1430. https://doi.org/10.1126/science.1208336

Rignot, E., Mouginot, J., & Scheuchl, B. (2017). Measures insar based Antarctica ice velocity map, version 2 [dataset]. National Snow and Ice Data Center Distributed Active Archive Center, https://doi.org/10.5067/D7GK8F5J8M8R

Schoof, C., & Hindmarsh, R. C. A. (2010). Thin-film flows with wall slip: An asymptotic analysis of higher-order flow models. *Quarterly Journal of Mechanics & Applied Mathematics*, *63*(1), 73–114. https://doi.org/10.1093/qjmam/hbp025

Smith, E. C., Baird, A. F., Kendall, J. M., Martin, C., Brisbourne, A. M., & Smith, A. M. (2017). Ice fabric in an Antarctic ice stream interpreted from seismic anisotropy. *Geophysical Research Letters*, *44*(8), 3710–3718. https://doi.org/10.1002/2016GL072093

Staroszczyk, R., & Morland, L. (2000). Plane ice-sheet flow with evolving orthotopic fabric. *Annals of Glaciology*, *30*, 93–101. https://doi.org/10.3189/172756400781820570

Thorsteinsson, T., Kipfstuhl, J., & Miller, H. (1997). Textures and fabrics in the GRIP ice core. *Journal of Geophysical Research*, *102*(C12), 26583–26599. https://doi.org/10.1029/97JC00161

Touzi, R., Lopes, A., Bruniquel, J., & Vachon, P. (1999). Coherence estimation for SAR imagery. *IEEE Transactions on Geoscience and Remote Sensing*, *37*(1), 135–149. https://doi.org/10.1109/36.739146

van der Veen, C. J., & Whillans, I. M. (1994). Development of fabric in ice. *Cold Regions Science and Technology*, *22*(2), 171–195. https://doi.org/10.1016/0165-232X(94)90027-2

Wang, Y., Thorsteinsson, T., Kipfstuhl, J., Miller, H., Dahl-Jensen, D., & Shoji, H. (2002). A vertical girdle fabric in the North GRIP deep ice core. *Journal of Glaciology*, *35*, 515–520. https://doi.org/10.3189/17275640278181730

Woodcock, N. (1977). Specification of fabric shapes using an eigenvalue method. *The Geological Society of America Bulletin*, *88*(9), 1231–1236. https://doi.org/10.1130/0016-7606(1977)88<1231:sofsua>2.0.co;2

Young, T. J., Martín, C., Christoffersen, P., Schroeder, D. M., Tulaczyk, S. M., & Dawson, E. J. (2021). Rapid and accurate polarimetric radar measurements of ice crystal fabric orientation at the Western Antarctic Ice Sheet (WAIS) Divide ice core site. *The Cryosphere*, *15*(8), 4117–4133. https://doi.org/10.5194/tc-15-4117-2021

Young, T. J., Schroeder, D. M., Jordan, T. M., Christoffersen, P., Tulaczyk, S. M., Culberg, R., & Bienert, N. L. (2021). Inferring Ice Fabric From Birefringence Loss in Airborne Radargrams: Application to the Eastern Shear Margin of Thwaites Glacier, West Antarctica. *Journal of Geophysical Research: Earth Surface*, *126*(5), e2020JF006023. https://doi.org/10.1029/2020JF006023